

Reversible-jump MCMC reveals binary black hole subpopulations with distinct redshift evolution

April Qiu Cheng^{1*}, Alexandre Toubiana^{2,3}, Sylvia Biscoveanu⁴,
Jonathan Gair⁵

¹Department of Astrophysical Sciences, Princeton University, 4 Ivy Lane, Princeton, NJ 08544, USA.

²Dipartimento di Fisica “G. Occhialini”, Università degli Studi di Milano-Bicocca, Piazza della Scienza 3, Milano, 20126, Italy.

³INFN, Sezione di Milano-Bicocca, Università degli Studi di Milano-Bicocca, Milano, 20126, Italy.

⁴Department of Physics, Princeton University, Princeton, NJ 08544, USA.

⁵Astrophysical and Cosmological Relativity, Max Planck Institute for Gravitational Physics (Albert Einstein Institute), Am Mühlenberg 1, Potsdam, 14476, Germany.

*Corresponding author(s). E-mail(s): aqcheng@princeton.edu;
Contributing authors: alexandre.toubiana@unimib.it;
sbisco@princeton.edu; jonathan.gair@aei.mpg.de;

Abstract

Analyses of the growing catalog of binary black hole (BBH) mergers observed by the LIGO-Virgo-KAGRA detectors are beginning to resolve features in their population-level mass, spin, and redshift distributions, revealing imprints of the astrophysical processes driving their formation and evolution. We present a novel method to search for subpopulations in the data using reversible-jump Markov chain Monte Carlo, providing interpretable results while making minimal prior assumptions. We find evidence for three subpopulations: a narrow subpopulation in primary mass at $\sim 10 M_{\odot}$ with preferentially aligned spins and unequal masses, consistent with isolated binary evolution; a subpopulation broadly distributed around $\sim 30 M_{\odot}$ with isotropically-distributed spins and a strong preference for equal mass ratios, consistent with dynamical formation in clusters; and a high-spin subpopulation spanning the continuum in mass, which we interpret as the confluence of multiple subdominant formation channels. When

we allow for the independent redshift evolution of each subpopulation, we find that the subpopulation encompassing the $10 M_{\odot}$ peak evolves more quickly than the $30 M_{\odot}$ subpopulation, with implications for the delay-time distribution and metallicity-dependent BBH formation efficiency. Our work lays the foundation for a novel data-driven framework to infer the formation mechanisms of BBHs.

1 Introduction

Among the most salient open questions in astrophysics is the formation mechanism(s) of binary black holes (BBHs). Different astrophysical formation channels are expected to produce BBHs with distinct signatures in the multidimensional parameter space defined by their masses, spin vectors, and redshifts. For example, tides in the stellar progenitors of mergers of isolated binaries are expected to efficiently align the progenitor spins to the orbital angular momentum, leading to component black holes with preferentially aligned spin vectors [1–9]; gas accretion will also align (or anti-align) the spin vectors in mergers of black holes (BHs) trapped in the disks of active galactic nuclei (AGN) [10–14]. On the other hand, mergers of BHs from dynamical interactions in a dense cluster are expected to have isotropically distributed spin orientations [8, 15–18], while those formed in stellar triples may have spins preferentially perpendicular to the orbital plane due to a combination of precession and Kozai–Lidov effects driven by the outer body [19–22]. For reviews of possible BBH formation pathways and their observational signatures, see e.g. [23–26].

We are now in a position to address this question using gravitational wave (GW) observations of coalescing BBHs by the LIGO-Virgo-KAGRA (LVK) Collaboration [27–31]. The release of the 4th Gravitational Wave Transient Catalog (GWTC-4) [32] has more than doubled the catalog size compared to its predecessor, providing significant insight into the structure of the underlying source population [33]. There is now increasing evidence for multiple subpopulations of BBHs, each with distinct mass, mass ratio, and spin properties, consistent with a population sourced by a mixture of formation channels [34–36].

Methods for looking for subpopulations in the data can be roughly grouped into *strongly-modeled* and *weakly-modeled* approaches. In the former, one typically describes the population as a mixture of astrophysically-motivated parametric functional forms, each representing a hypothesized formation channel [34–44], and infers their relative rates; one can also fit the data directly to the output of population synthesis models [38, 45, 46]. While such strongly parameterized models offer direct astrophysical interpretability, they risk imposing structure that is absent from the data, or hiding structure that is not anticipated by the model [47]. On the other hand, weakly-modeled approaches make only minimal assumptions about the population distribution (e.g., that it is smooth), instead letting the data drive the shape of the inferred population [36, 41, 48–50, 50–58]. The increased flexibility comes at the cost of additional model and computational complexity and reduced astrophysical interpretability. In particular, the identification of subpopulations typically requires some

heuristic extra processing steps, such as dividing the population in parameter space by eye [36, 58].

In this work, we present a novel “best of both worlds” search for subpopulations using reversible-jump Markov chain Monte Carlo (RJ MCMC) [59], which simultaneously performs Bayesian model comparison between models of varying complexity along with inference on the model parameters. RJ MCMC has previously been applied to the analysis of the BBH population by [54], which used reversible-jump to optimize the complexity of one-dimensional semi-parametric and non-parametric models, and later by [60], which extended it to multidimensional non-parametric inference. This work is motivated by the following idea: because the number of subpopulations within the BBH population is unknown, RJ MCMC is a natural and computationally efficient framework to identify them without over-fitting the data. That is, for a mixture model of n suitably flexible subpopulations, RJ MCMC finds the best n along with the features of each subpopulation. Because our model still consists of a mixture of physical model components, rather than a purely descriptive representation of the data, we retain the advantage of interpretability over non-parametric methods. In short, this is a data-driven method with the clarity of a parametric approach.

Applying this framework to the GWTC-4 data, we robustly identify three subpopulations consistent across multiple variants of population models. We find 1) a subpopulation at $m_1 \approx 10 M_\odot$ with small positive χ_{eff} and a mild preference for unequal-mass pairings, consistent with isolated binary evolution; 2) a broad peak at $m_1 \sim 30 M_\odot$ with a χ_{eff} distribution centered at zero and a strong preference for equal-mass pairings, consistent with dynamical assembly; and 3) a high-spin continuum extending to high masses with a positive-mean, broad χ_{eff} distribution, which includes the exceptional events of the catalog. We also find evidence for differences in the evolution of different subpopulations with redshift, implying a short delay-time distribution and inefficient binary progenitor formation above moderate metallicities for the subpopulation including the $10 M_\odot$ peak and the continuum.

2 Three binary black hole subpopulations

Population inference of GW data is typically performed using hierarchical Bayesian inference, in which one fits a population model to the source parameters θ representing an individual binary in the catalog, which are in turn inferred from the GW strain data. The key astrophysical ingredient is the population model, which we briefly describe below; details of our methodology can be found in Section 6.

We model the BBH population as a mixture of n components on the 4-dimensional parameter space $\theta = [m_1, q, \chi_{\text{eff}}, z]$ consisting of the primary mass, mass ratio, effective aligned spin, and redshift, such that the differential merger rate per unit detector time

t is given by

$$\begin{aligned} \frac{dN}{d\theta dt}(\{\boldsymbol{\lambda}\}, \boldsymbol{\Lambda}) &= \sum_{k=1}^n \frac{dN_k}{dt d\theta}(\boldsymbol{\lambda}_k, \boldsymbol{\Lambda}) \\ &= \frac{dV_c}{dz} \sum_{k=1}^n \frac{\mathcal{R}_{0,k} \psi(z|\boldsymbol{\Lambda})}{1+z} p_k(m_1, q, \chi_{\text{eff}}|\boldsymbol{\lambda}_k, \boldsymbol{\Lambda}), \end{aligned} \quad (1)$$

where each subpopulation k has a local ($z = 0$) merger rate $\mathcal{R}_{0,k}$ and a distribution $p_k(\boldsymbol{\theta}|\boldsymbol{\lambda}_k, \boldsymbol{\Lambda})$ dependent on its subpopulation parameters $\boldsymbol{\lambda}_k$ as well as global population parameters $\boldsymbol{\Lambda}$ shared between all subpopulations. For example, in our default population model we model the source-frame merger rate as a power-law

$$\psi(z|\gamma) = (1+z)^\gamma \quad (2)$$

with index $\gamma \in \boldsymbol{\Lambda}$ shared between all subpopulations. This assumption can be relaxed, the results of which we will discuss in Section 4. In our framework, n is a free parameter; RJ MCMC returns posterior samples on $\{\boldsymbol{\lambda}\}$ and $\boldsymbol{\Lambda}$ for all models of different n , with the number of samples proportional to the relative evidences, or equivalently, the Bayes factors (\mathcal{B}).

To verify the robustness of our results, we search for subpopulations across several variants of population models, which differ primarily in the functional form of the mass distribution. In our default population model (**skewt**), we model the primary mass distribution of each subpopulation as a skew-t distribution, which is a flexible, 4-parameter distribution that can accommodate both asymptotic power-law and Gaussian behavior, and can broadly capture the features of most smooth, unimodal distributions. We compare these results to a mixture model of power-laws and Gaussians (**NPLNP**), which is similar to common strongly parameterized models in the literature [33, 61], except here the number of components is not fixed. In both of these cases, we model the conditional mass ratio distribution $p(q|m_1)$ as a truncated Gaussian. We also employ a population model with an alternate parameterization of the mass ratio (**skewt_ID**), in which both BHs in the binary are drawn from the same BH mass distribution. Their pairing is described by a correlation coefficient $-1 < \rho < 1$, where $\rho = 0$ describes independent BH pairing, and $\rho = 1$ and $\rho = -1$ are extremes where the masses are perfectly correlated (i.e., mass ratio is always equal) and perfectly anti-correlated (in quantile, i.e., the cumulative density functions (CDFs) evaluated at the two masses always sum to 1), respectively. This parameterization has the advantage of reduced complexity compared to the 2 parameters of a Gaussian.

For each population model, we show results from the most preferred model, which is 3 components for **skewt** and **skewt_ID**, and 2 power-laws + 1 Gaussian for **NPLNP**. As we discuss further below, this model is only weakly preferred over a 2-component model. Bayes factors between the models of different complexity within each population model can be found in Table 2.

Fig. 1 shows draws from the 1D marginalized distributions of each subpopulation as well as their total, inferred from our default **skewt** population model; the corresponding results for the **skewt_ID** and **NPLNP** population models can be found in

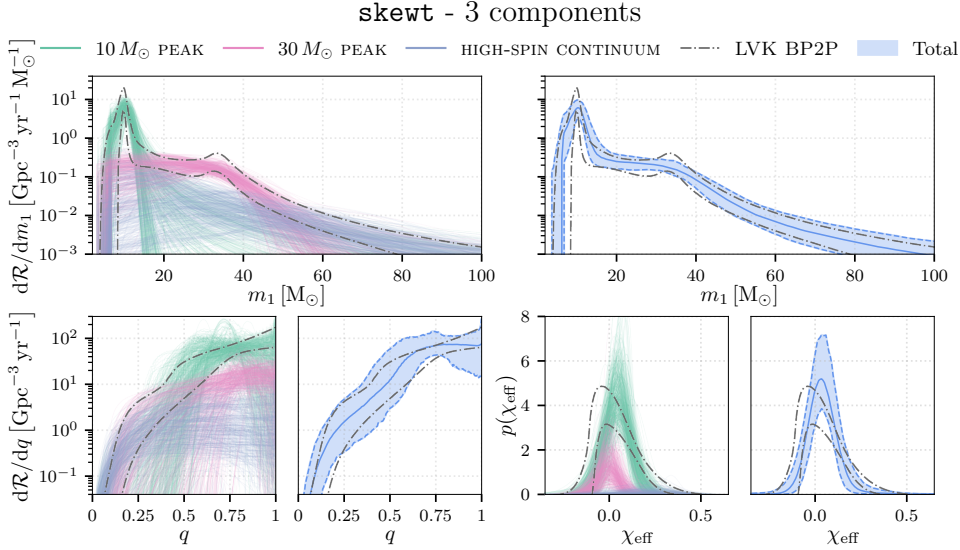


Fig. 1: Posterior sample draws for differential merger rates as a function of primary mass, mass ratio and effective spin at $z = 0.2$ in our fiducial **skewt** 3-component model. The 10 M_⊙ peak, 30 M_⊙ peak, and high-spin continuum subpopulations are plotted in green, pink, and indigo, respectively, while the posterior median and 90% credible intervals of their total are plotted in shaded blue on the right for each parameter. The corresponding curves for the BROKEN POWER-LAW + 2 PEAKS population model of the LVK analysis [33], which uses a skew-normal model for χ_{eff} and a power-law distribution for the mass ratio, are plotted for comparison (dashed-dot gray).

Extended Data Fig. 2. The marginalized distributions are largely consistent with the LVK analysis [33]. In m_1 , we recover a sharp peak at 10 M_⊙, a bump around 30 M_⊙, and a power-law-like tail at high masses. While our NPLNP analysis prefers 1 power-law + 2 Gaussians compared to the preferred BROKEN POWER-LAW + 2 PEAKS model in the LVK analysis, this difference is attributable to the fact that including an extra power-law component at the break incurs a heavier Occam’s razor penalty, as each subpopulation has independent mass ratio and spin distributions [33]. Our inferred mass ratio distribution is consistent with peaking at $q \sim 0.7 - 1$, while the LVK results more strongly favor a mass ratio distribution that peaks at equal masses. In contrast to the LVK χ_{eff} population model, which specifically allows and finds evidence for skewness [62], our population model uses a symmetric χ_{eff} distribution, so such an asymmetry would need to be constructed from the overlap of multiple subpopulations. Where subpopulations overlap, there is greater degeneracy between the relative contributions from each subpopulation, as shown by the fact that the total population distribution is better constrained than the distributions of each subpopulation.

The 3 identified subpopulations are consistent across all population models that we test. We compare the results of the **skewt** and NPLNP population models in Fig. 2. Here, we plot the posterior differential merger rate as a function of m_1 and χ_{eff} , the two best

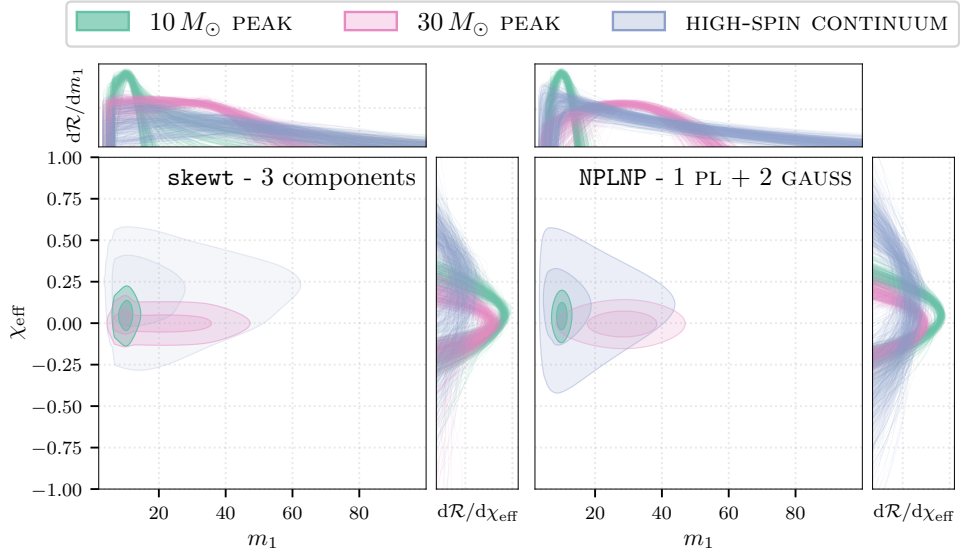


Fig. 2: 50% and 90% contours of the median posterior $d\mathcal{R}^k/dm_1 d\chi_{\text{eff}}$ for each sub-population k , evaluated at $z = 0.2$; opacity of the shading corresponds to the relative rates of the subpopulations. We show the most preferred model of the **skewt** (left) and **NPLNP** (right) population models, with 3 subpopulations in both. Corresponding posterior sample draws from the marginalized 1D distributions (in log-scale) are shown in the top and side panels.

measured parameters in the parameter space θ ; different subpopulations occupy visibly distinct regions of parameter space. The subtle differences between the population models illustrate the impact of strongly parameterized models. Comparing the two m_1 distributions in the top insets, we can see that the **NPLNP** model forces the high-spin continuum subpopulation to peak at lower masses due to its parameterization as a power-law, and forces the $30 M_\odot$ peak to drop off at small masses due to its parameterization as a Gaussian. In contrast, inference with the **skewt** population model finds significant support around $m_1 \lesssim 10$ for the $30 M_\odot$ subpopulation. In turn, this causes subtle differences in the resulting χ_{eff} and mass ratio distributions of each subpopulation. Nonetheless, the fact that both population models are still qualitatively consistent lends credibility to our results.

We now describe the three subpopulations as follows:

$10 M_\odot$ peak. This is a narrow subpopulation centered at $m_1 \approx 10 M_\odot$ with small positive χ_{eff} , consistent with isolated formation channels producing BBHs with spins aligned with the orbital angular momentum. We plot this subpopulation in green throughout this paper.

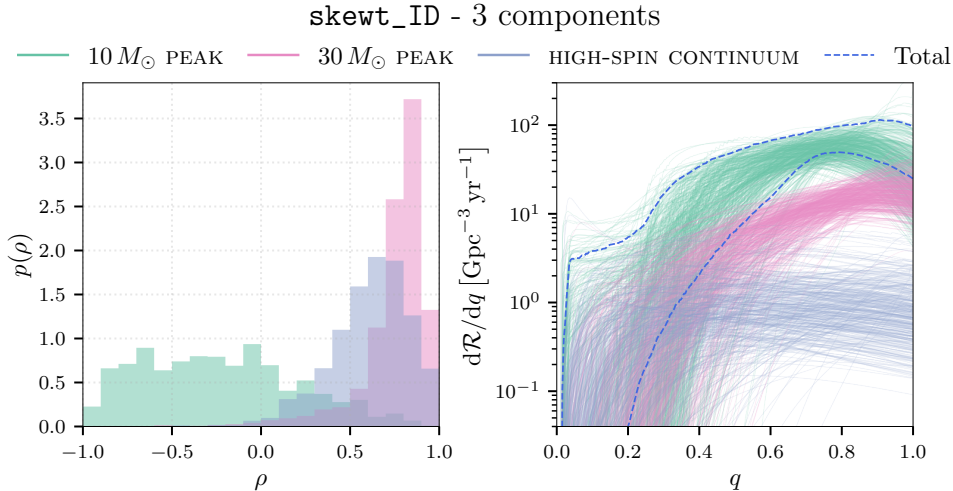


Fig. 3: Posteriors of the mass pairing correlation coefficient ρ for each subpopulation (left) and the corresponding differential merger rate as a function of q at $z = 0.2$, inferred from the `skewt_ID` population model. In the right panel, colored curves are random posterior draws of the marginal differential merger rate on q for each subpopulation, with the 90% credible interval of the total distribution plotted in dashed blue. The 10 M_{\odot} peak is consistent with uncorrelated pairing, resulting in a mass ratio distribution peaked away from $q = 1$, while the 30 M_{\odot} peak shows a strong preference for equal mass ratios.

The peak of the primary mass distribution is* $10.3_{-1.4}^{+1.4} M_{\odot}$ ($10.0_{-0.9}^{+1.0} M_{\odot}$) in the `skewt` (NPLNP) population model. The mean of the χ_{eff} distribution is $\mu_{\chi} = 0.05_{-0.04}^{+0.04}$ ($0.04_{-0.03}^{+0.03}$), with $\mu_{\chi} > 0$ measured at 98.2% (98.6%) credibility. This is also the largest subpopulation of the three, with a branching fraction of $0.77_{-0.12}^{+0.12}$ ($0.77_{-0.18}^{+0.08}$) and a merger rate of $14.6_{-4.9}^{+7.0}$ ($14.7_{-5.5}^{+6.7}$) $\text{Gpc}^{-3} \text{yr}^{-1}$.

Because the masses of BBHs in this subpopulation are confined within a narrow mass range, mass ratios are not well measured. Nonetheless, there is tentative evidence that this subpopulation supports unequal mass ratios more than the rest of the population. As seen in the left panel of Fig. 3, this subpopulation shows the strongest support for independent pairing of BH masses, with $\rho < 0.38$ with 90% credibility in the `skewt_ID` population model. The induced marginal $p(q)$ distribution, shown in the right panel, peaks at $q_{\text{peak}} = 0.80_{-0.16}^{+0.13} < 1$. However, this signature is weaker in the default population model, possibly due to the increased model complexity: the posterior on the peak of the conditional mass ratio distribution μ_q deviates only weakly from the prior, although still consistent with unequal mass ratios ($\mu_q = 0.55_{-0.40}^{+0.38}$).

The properties of this subpopulation—a narrow mass peak, a small but robustly positive mean χ_{eff} , a preference for unequal pairings, and the bulk of the overall

*In this paper, all quoted uncertainties correspond to the median and 90% central credible intervals unless otherwise specified.

merger rate—are collectively consistent with an isolated field binary evolution origin. The small positive mean χ_{eff} we infer is consistent with a general isolated binary formation scenario: spins are generally expected to be aligned with the orbital angular momentum, and tidal spin-up of the tidally-locked second-born progenitor naturally produces small but positive χ_{eff} , even if the first-born BH is born slowly spinning [63–66].

A peak at $10 M_{\odot}$ has been found previously in the literature [49, 67–69] and interpreted in several isolated formation scenarios. The stable mass transfer (SMT) formation scenario predicts a peak around this mass range, as it is inefficient at producing mergers below $\sim 9 - 10 M_{\odot}$. This is because orbits must shrink via the direct loss of mass carrying away angular momentum during the second mass-transfer phase, as opposed to drag forces present in a binary common envelope during dynamically unstable mass transfer, and such orbital tightening is inefficient for lower mass BBHs [70, 71]. SMT can also explain the preference for unequal masses that we find for this subpopulation, as unequal mass BBHs are more likely to shrink their orbits during the mass transfer episode [72], with mass ratios predicted to peak around $q \sim 0.6 - 0.8$ [73, 74]. A peak around $9 M_{\odot}$ has also been predicted in the mass spectrum of BHs formed from binary-stripped stars. Core compactness reaches a local maximum in that mass range as a consequence of a transition to neutrino-dominated burning, causing decreased explodability and hence increased probability of BH formation [75–77]. Finally, ref. [69] targeted the $10 M_{\odot}$ peak as a separate subpopulation, interpreting the peak as failed-supernova BHs forming from direct collapse in a narrow progenitor-mass range [78]. They also find a mass ratio and χ_{eff} distribution of the subpopulation different from the rest of the population, consistent with our findings.

30 M_{\odot} peak. This subpopulation has m_1 broadly distributed around $30 M_{\odot}$, a χ_{eff} distribution centered at 0, and a strong preference for equal mass ratios, consistent with dynamical formation scenarios in clusters. We plot this subpopulation in pink throughout this paper.

Quantitatively, this subpopulation peaks in primary mass at $23.7_{-13.3}^{+10.2}$ ($28.1_{-2.8}^{+3.6}$) in the `skewt` (NPLNP) population model, although in `skewt` the peak is more akin to a plateau with a fall-off starting around $\sim 30 M_{\odot}$, as seen in the top left panel of Fig. 1. The mean of the χ_{eff} distribution is squarely zero, with $\mu_{\chi} = 0.00_{-0.04}^{+0.04}$ ($-0.01_{-0.04}^{+0.03}$). Fig. 3 shows that this subpopulation has the strongest preference for equal mass pairings out of all the subpopulations, with $\rho = 0.80_{-0.44}^{+0.13} \sim 1$ in the `skewt_ID` population model and $\mu_q > 0.71$ (0.76) in `skewt` (NPLNP) at 90% credibility. This is the second-most populous subpopulation, with a branching fraction of $0.19_{-0.11}^{+0.12}$ ($0.12_{-0.05}^{+0.07}$) and merger rate of $3.7_{-2.1}^{+2.6}$ ($2.3_{-1.0}^{+1.5}$) $\text{Gpc}^{-3} \text{yr}^{-1}$.

Isotropic spin orientations are a robust signature of formation scenarios where mergers are formed dynamically in a globular or nuclear star cluster, which implies a χ_{eff} distribution symmetric about zero [79]. Furthermore, mass segregation and the larger interaction cross-section of heavier BHs both favor dynamical pairings at high mass and near-equal mass ratios [80, 81]. Moreover, some simulations of dense star clusters are able to predict the overdensity around $30 M_{\odot}$ as well as the measured merger rate [82–84], given sufficiently high cluster densities. While first-generation

mergers in AGN disks are also predicted to have a χ_{eff} distribution centered at zero [85], they do not predict a strong preference for equal mass ratios.

The pile-up of BBHs around this mass-range has been well-known even from early phenomenological analyses of the BBH mass spectrum [61, 86]. Other analyses have also found the equal-mass and/or isotropic spin properties of the BBHs in this mass range, including both flexible [36] and strongly-parameterized mixture models [34, 35] and interpreted this subpopulation as dynamically assembled.

High-spin continuum. This is a small subpopulation spanning the continuum in primary mass, including a tail out to high masses, which we plot in indigo throughout this paper. Note that the existence of this subpopulation is only mildly preferred by the data when it is modeled by a skew-t distribution compared to a 2-component model, with $\mathcal{B} = 1.3$ (2.7) in the `skewt` (`skewt_ID`) population models; see Table 2. In the 2-component model, this continuum is absorbed into the peak at $10 M_{\odot}$. However, an analogous 2-component model is disfavored in the NPLNP analysis with $\mathcal{B} = 0.08$, which could be a consequence of the decreased flexibility compared to the `skewt` population model.

Due to the wide range of masses spanned by this subpopulation, it naturally allows for the most extreme mass ratios. As seen in Fig. 2, it also has a much broader χ_{eff} distribution than the other two subpopulations centered at a significantly positive value. Quantitatively, the χ_{eff} distribution is centered at $\mu_{\chi} = 0.23^{+0.17}_{-0.18}$ ($0.11^{+0.16}_{-0.12}$) in the `skewt` (NPLNP) population model. It is also useful to examine the 90% central interval spanned by the χ_{eff} Gaussian; we find $\chi_{\text{eff}}^{5\%} = 0.00^{+0.29}_{-0.40}$ ($-0.18^{+0.27}_{-0.30}$) and $\chi_{\text{eff}}^{95\%} = 0.46^{+0.17}_{-0.12}$. Thus, while a χ_{eff} distribution with entirely non-negative support is neither significantly favored nor ruled out, this subpopulation confidently supports very positive values of $\chi_{\text{eff}} \sim 0.4$. This is the smallest subpopulation, with a branching fraction of $0.02^{+0.08}_{-0.02}$ ($0.11^{+0.20}_{-0.08}$) and a local merger rate of $0.5^{+1.6}_{-0.5}$ ($2.1^{+4.3}_{-1.5}$) $\text{Gpc}^{-3} \text{yr}^{-1}$.

Unlike the other two subpopulations, this subpopulation resists an obvious astrophysical interpretation. Hierarchical mergers in stellar clusters, where one or both of the BHs are formed from a previous merger, do produce higher-mass BBHs and large spins, but the expectation is for χ_{eff} to be symmetric about zero with $|\chi_{\text{eff}}| \lesssim 0.5$ [8, 79, 87, 88] due to the prediction for the BH spin orientations to be isotropic with respect to the orbital angular momentum. Instead, we find that $\mu_{\chi} > 0$ with 99% (93%) credibility. This is in contrast with the zero-centered distributions inferred for the high-mass BBHs in [35, 37, 89], who have interpreted those BBHs as hierarchically merged in clusters. As we will discuss in Section 3, while many events identified as hierarchical merger candidates in previous works do fall into this subpopulation, the χ_{eff} distribution of this subpopulation is inconsistent with consisting entirely of cluster hierarchical mergers. Several other formation channels therefore plausibly contribute to this subpopulation. The inferred properties of this subpopulation are consistent with the chemically homogeneous evolution (CHE) of low-metallicity stars, predicted to produce massive, near-equal-mass BBHs with high positive aligned spins [6, 7, 90, 91], as well as hierarchical mergers in the disks of AGN, where gas torques can partially align spins and produce a χ_{eff} distribution skewed to positive values [12, 44, 92, 93]. A high-mass subpopulation with aligned spins was found in [44] and also interpreted as hierarchical mergers in AGN disks. We therefore interpret this subpopulation as

a residual “catch-all” component that naturally absorbs diverse exceptional events in our framework, rather than as the signature of any single formation channel. Further observations, and possibly the inclusion of more spin parameters in our analysis, may be able to resolve the formation channels that constitute this subpopulation.

Besides its spin properties, another indication of a hierarchical origin for a BBH is if it populates the BH mass gap expected from pair-instability supernovae (PISNe). Recently, ref. [94] has found evidence for the PISN mass gap in the secondary mass distribution. Using a variant of our default population model, we investigate and verify the presence of a sharp drop-off in the secondary mass distribution. The results can be found in Extended Data Fig. 1.

3 Individual events

Next, we examine the posterior probability that each individual observed event belongs in each subpopulation, and where each event is located in parameter space. Fig. 4 shows the default `skewt` 3-component model’s population-weighted posteriors of all analyzed events in m_1 and χ_{eff} . Events which are likely ($> 75\%$) to belong to one subpopulation are color-coded accordingly; otherwise, they are plotted in gray.

We identify these events in Fig. 5, which shows the default model’s subpopulation probabilities of the top 10 most confident events in each subpopulation, as well as the top 10 most ambiguous events. We then compare this to the subpopulation probabilities of the NPLNP 1 power-law + 2 Gaussians model of the same events, which we plot to the right. All events that are confidently detected in each subpopulation in the `skewt` population model are also confidently detected in the NPLNP model, supporting the robustness of these subpopulations.

The high-spin continuum subpopulation contains many of the exceptional events in the catalog in at least one of our population models. These include GW190412 [95], which is notable for its highly asymmetric masses, as well as GW231123 [96], which is both notable for their high masses and spins. GW190412 has also been identified as a candidate for an AGN disk-driven hierarchical merger origin [97–99], and both CHE [91] and hierarchical AGN-disk mergers [100, 101] have been proposed as formation scenarios for GW231123. Additionally, the primary spin of GW190412 is too low [102] and the spins of GW231123 too high [103] for a cluster hierarchical merger scenario. Nonetheless the high-spin continuum subpopulation does contain most of the events identified as candidates for hierarchical mergers in previous works, including GW190517_055101, GW231028_153006 [37], GW231118_005626 [43], GW190519_153544, GW190620_030421, and GW190706_222641 [39]. This further emphasizes the ambiguous astrophysical interpretation of this subpopulation.

We can also examine the population-weighted posteriors of the O4b exceptional events GW241011 and GW241110 [104, 105], which we show in Fig. 4. These events are identified as the most likely candidates for containing a BH with a hierarchical origin [37, 43, 104], although we do not include them in our population analysis (as doing so would constitute essentially adding two events to the population by hand). With the `skewt` (NPLNP) population model, we find that the probability that GW241011 belongs in the high-spin continuum is 90.4% (99.9996%), while the corresponding probability

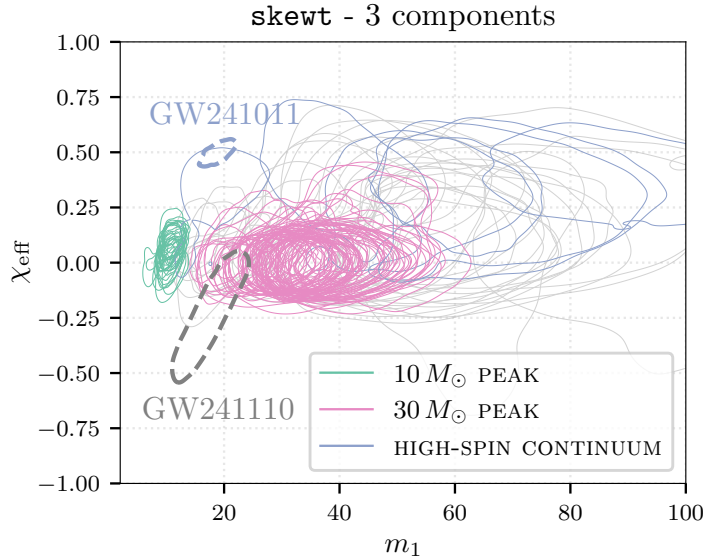


Fig. 4: 90% contours in primary mass and effective spin of the population-weighted posteriors of the 153 GWTC-4 events along with GW241011 and GW241110, using the results of our default `skewt` analysis. Events with $> 75\%$ probability of belonging to a subpopulation are color-coded accordingly, and otherwise plotted in gray. The clustering of the three subpopulations is clearly visible.

for GW241110 is 35% (91%). This is consistent with the ambiguous astrophysical interpretation of this subpopulation, especially in the `skewt` population model. It is important to note that because both events have exceptional spins, including them in the population analysis has the potential to significantly change the properties of this subpopulation. Furthermore, because we only use χ_{eff} rather than the full component spin vectors, we are not sensitive to more specific predictions of the hierarchical merger channel, such as the expectation for one or more of the component BHs to have spin magnitude $\chi \approx 0.7$ [106, 107]. Reapplying our framework to the full O4b catalog, and possibly expanding to more spin parameters, will constitute an important next step for finding a robust subpopulation of hierarchical mergers.

4 Correlations

4.1 Different subpopulations evolve differently in redshift

In our default model, we assumed a global rate evolution $\psi(z|\gamma)$, where γ is the global power-law index, shared between all subpopulations. We relax this assumption in the `skewt_z` population model, allowing each subpopulation to have its own γ . We recover the same subpopulations as above, except now the 2-component model is slightly favored over the 3-component model with $\mathcal{B} = 1.6$, likely due to the increase

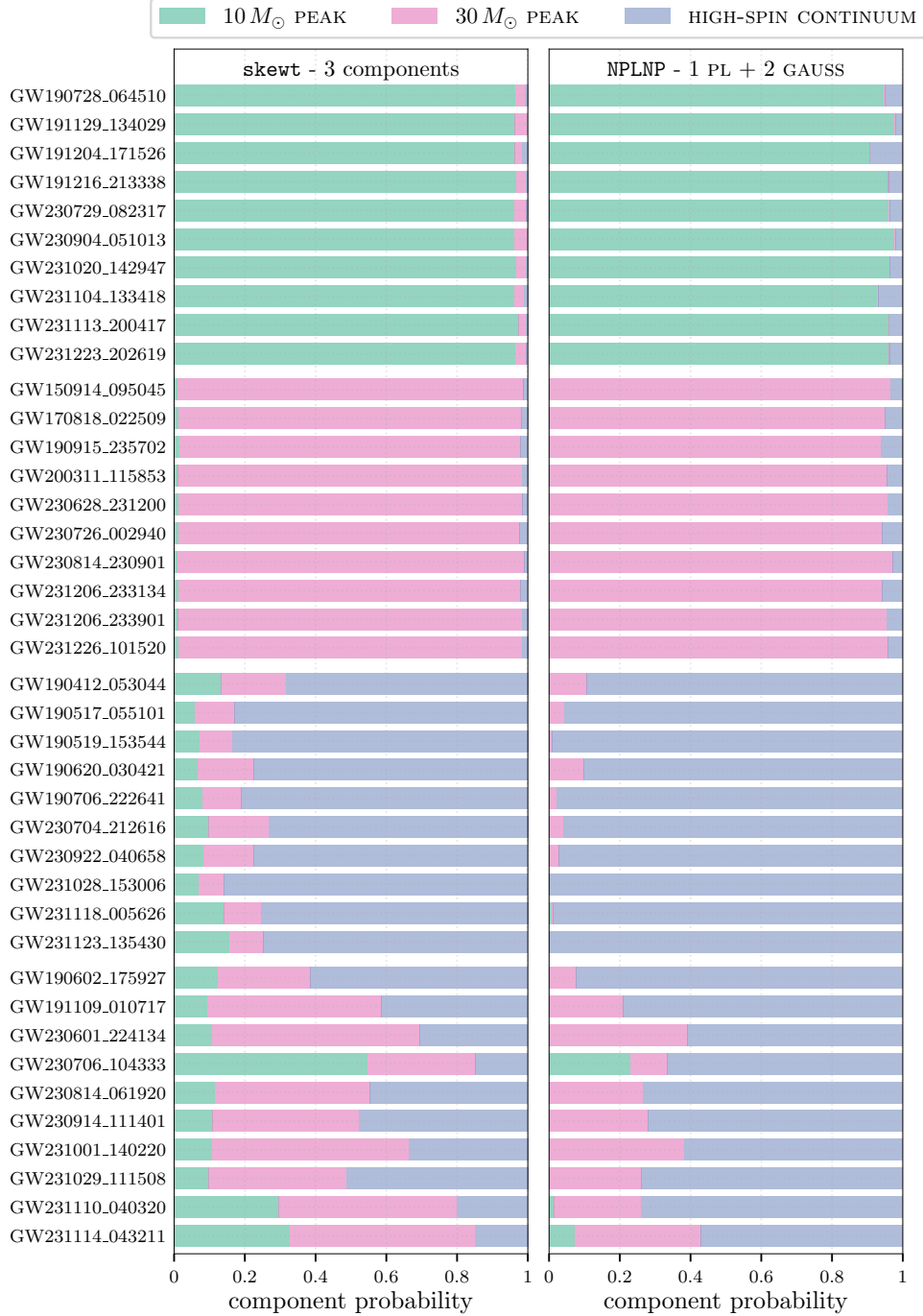


Fig. 5: Probabilities of individual events belonging to each subpopulation for the *skewt* 3-component model (left) and NPLNP 1 power-law + 1 Gaussian model (right). We plot in blocks of 10 the top events of each *skewt* subpopulation, as well as the model's most ambiguous events at the bottom, which we define as the events with the smallest Kullback-Leibler divergence from a uniform distribution between the 3 subpopulations. Events are organized chronologically within each block.

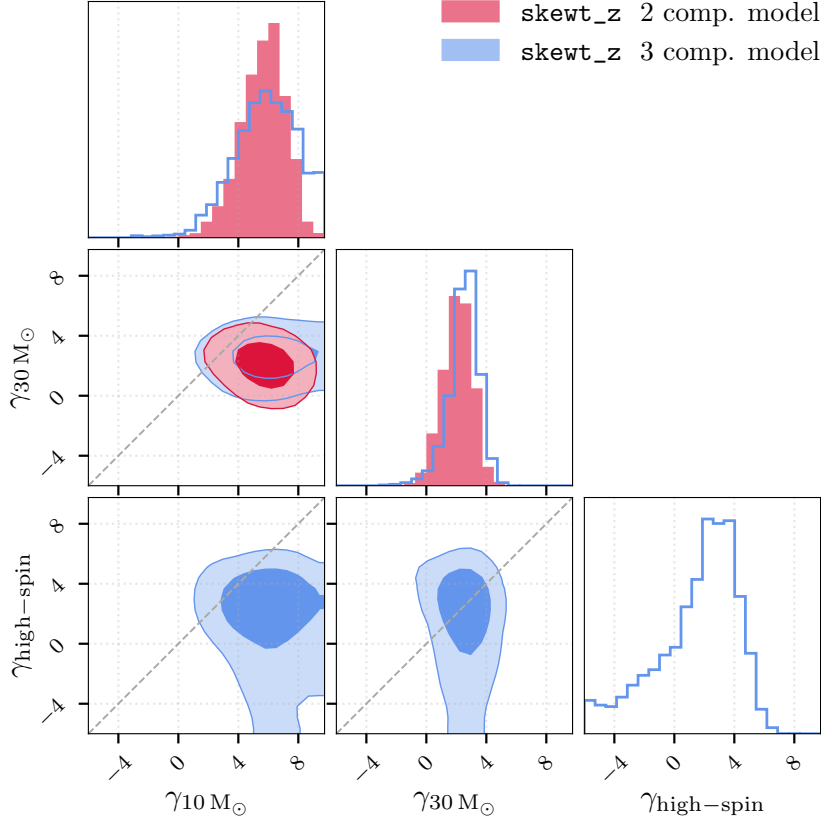


Fig. 6: Posteriors on the power-law index γ of the source-frame rate evolution with redshift of our different subpopulations for the 2-component model (red) and the 3-component `skewt_z` model. The diagonal gray line demarcates where $\gamma_A = \gamma_B$ for any subpopulations A, B . In both models, the $10 M_\odot$ peak subpopulation prefers a faster rate evolution than the other component(s).

in the parameter space. The top panels of Fig. 7 show draws from the marginalized m_1 population distributions of both models. As before, the $10 M_\odot$ peak combines with the high-spin continuum in the 2-component model, whereas the 3-component model distributions are statistically consistent with those of the default `skewt` population model.

Fig. 6 shows a corner plot on γ of each subpopulation for both the 2-component and 3-component models. We find that the $10 M_\odot$ peak favors a significantly faster rate evolution, with $\gamma = 5.7^{+2.1}_{-2.8}$ ($6.0^{+3.2}_{-3.7}$) in the 2-component (3-component) model, compared to $\gamma = 3.0^{+0.9}_{-1.2}$ of the `skewt` inference which assumes a global rate evolution, consistent with the LVK’s inference. Compared to the $30 M_\odot$ peak subpopulation, $\gamma_{10 M_\odot} > \gamma_{30 M_\odot}$ at 94.6% (92.2%) credibility.

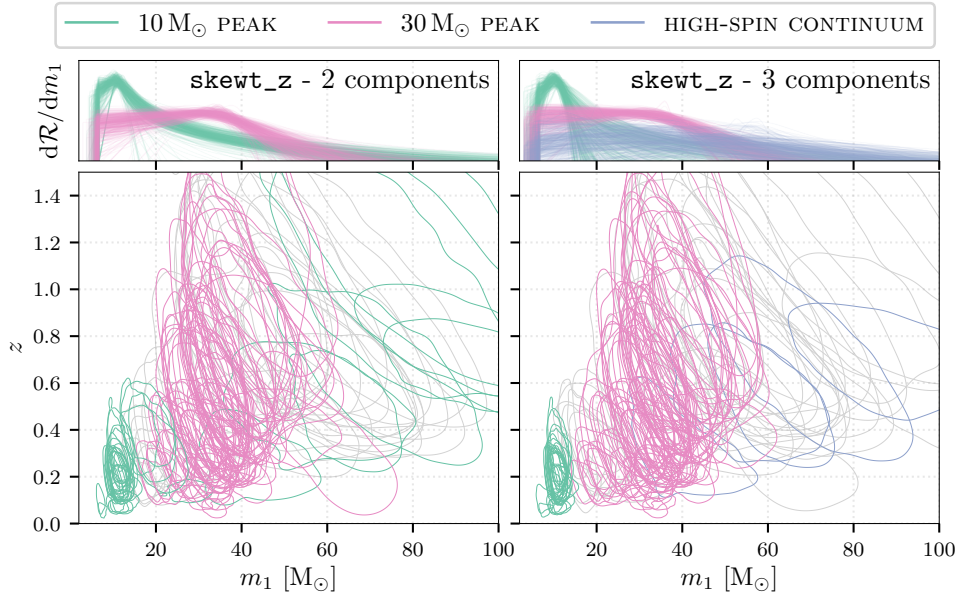


Fig. 7: Population-weighted posteriors color-coded by subpopulation as in Fig. 4, except here we plot m_1 and z of the 2-component (left) and 3-component (right) models of the `skewt_z` population model. The top inset shows posterior draws of the rate of each subpopulation at $z = 0.2$ as a function of m_1 . Because the continuum is included in the $10 M_\odot$ peak in the 2-component model, the subpopulation includes events at high masses and high redshifts.

The main implication of this result is that the $10 M_\odot$ peak and continuum will dominate as we go to higher redshifts with respect to the $30 M_\odot$ peak. Of course, this claim is only robust if events belonging to the $10 M_\odot$ peak provide information at high redshifts. It is therefore instructive to inspect the population-weighted posteriors of the events, which we show in Fig. 7. As seen in the left panel, the $10 M_\odot$ peak subpopulation is still informed by events at higher redshifts due to the fact that it extends to the high-mass continuum in the 2-component model, and therefore events around $10 M_\odot$ as well as events in the continuum have evidence for a fast redshift evolution. Indeed, evidence for a faster redshift evolution of a subpopulation of high-mass, highly-spinning BBHs has been found in previous works using more strongly parameterized models tailored to search for specific correlations [108, 109]. On the other hand, the faster redshift evolution of a re-analysis of selected low mass events have also found a faster redshift evolution [58].

Expanding on this idea, we can define a “maximum informative redshift” of each subpopulation as the greatest median population-weighted posterior redshift of any event which likely ($> 75\%$) belongs in the subpopulation. In Fig. 8, we plot the source-frame redshift evolution of each subpopulation, truncating the shading at the

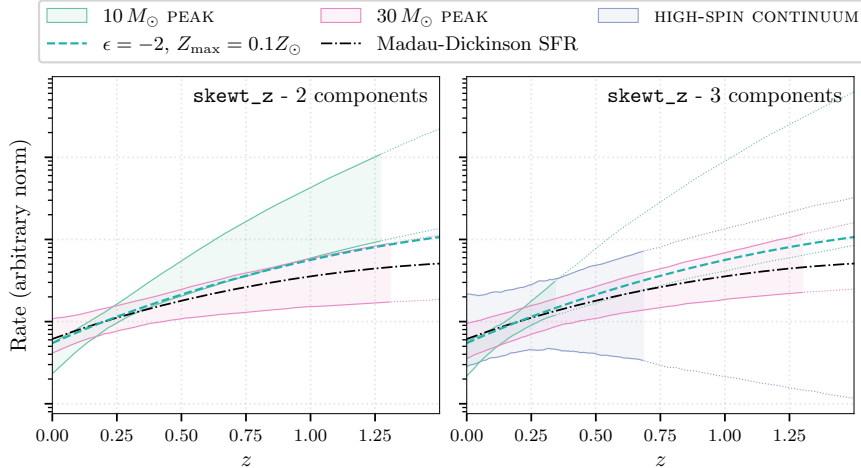


Fig. 8: Source-frame BBH merger rate as a function of redshift for each subpopulation, as well as the theoretical prediction for our simplified model with $p(t_d) \propto t_d^\epsilon$ and inefficient BBH formation above Z_{\max} (turquoise dashed line). The dash-dot black line shows our fiducial Madau-Dickinson star formation history. Posterior draws from the population model are normalized to their median rate at $z = 0.2$, and the theoretical merger history is normalized to its value at $z = 0.2$. As described in the text, the truncation of the shaded regions corresponds to the redshift beyond which the subpopulation has no redshift information from the data.

maximum informative redshift of each subpopulation. We show the resulting m_1 and χ_{eff} distributions at different redshifts in Extended Data Fig. 3.

The fast redshift evolution of the $10 M_\odot$ peak is nontrivial to explain with the standard picture of the BBH merger rate following the star formation history with some delay time. Following [110], we consider a model in which the BBH merger rate follows the Madau-Dickinson star formation history $\psi_{\text{MD}}(z)$ [111] with a power-law delay-time distribution $p(t_d) \propto t_d^\epsilon$ and inefficient BBH formation above a cutoff metallicity Z_{\max} . Thus, the BBH source-frame birth rate of BH binaries is proportional to $\psi_{\text{MD}}(z) F(Z_{\max}; z)$, where $F(Z_{\max}; z)$ is the fraction of star formation occurring below metallicity Z_{\max} , adopting the analytic prescription in ref. [112].

We test a grid of combinations of ϵ and Z_{\max} and compare the predicted rate evolution to the rate evolution inferred for our subpopulations. Because $\gamma \approx 6$ is significantly faster than the best-fit star-formation history (which has $\gamma = 2.7$ and a turnover at redshift 1.9, well beyond the majority of events in the catalog), we find that attempting to match the constraints inferred from the preferred two-component model requires adopting extremely short delay-time distributions together with a maximum metallicity for efficient BBH formation well below solar ($Z_{\max} \lesssim 0.1 Z_\odot$). Even in these relatively extreme scenarios, however, we still struggle to reproduce the inferred constraints for $z \gtrsim 1$. This is illustrated by the dashed red line in Fig. 8, showing the rate computed from $\epsilon = 2$ and $Z_{\max} = 0.1 Z_\odot$, which in the 2-component model

(left panel) is barely consistent with the lower edge of the 90% credible interval of the $10 M_{\odot}$ peak + continuum subpopulation. Slower delay times, introducing some minimum t_d , or a larger Z_{\max} all predict a rate evolution inconsistent with that of the $10 M_{\odot}$ peak and continuum.

In the 3-component model (right panel), although a steeper evolution for the $10 M_{\odot}$ peak is still preferred, the posteriors on γ are broader, due to the increase in model complexity and a decrease in the number of events per subpopulation. Thus, the power-law index for the $10 M_{\odot}$ peak is compatible with that of the $30 M_{\odot}$ peak within error bars, and in this model no constraints are placed on the delay time distribution or cutoff metallicity, especially since the faster rate evolution of the $10 M_{\odot}$ peak is confined to low redshifts of $z \lesssim 0.3$.

4.2 Correlations including spins

Previous works have found a broadening of the χ_{eff} distribution with redshift [109, 113] and a correlation between mass ratio and χ_{eff} [114–116], although evidence for the latter has become more ambiguous in the latest dataset [33]. We find no strong evidence for either of these correlations in our analysis, which we show in Extended Data Figs. 3 and 4. Our results suggest that the broadening of the χ_{eff} distribution with redshift is either driven by an intrinsic evolution of the BH spin distribution, or by subpopulations with more complex redshift evolution than can be accommodated by a power law (e.g. subpopulations localized within a narrower range of redshifts). This stands in contrast with the results of ref. [109]; we note, however, that their analysis included the two remarkable O4b events GW241110 and GW241011, and employed a population model specifically designed to target a subpopulation of hierarchical mergers.

5 Conclusion

The origin of BBHs is one of the central questions in modern astrophysics. Active theoretical efforts are ongoing to answer this question, and a wide range of formation channels have been proposed. These include isolated binary evolution involving orbital tightening through stable or unstable mass transfer, dynamical assembly in dense stellar clusters or triple systems, CHE in close, low-metallicity binaries, hierarchical mergers of previous merger remnants, gas-assisted mergers in the disks of AGN, and more. The joint distributions of masses, spins, and redshift predicted by these models differ, and therefore provide a means to disentangle the relative contributions of each formation channel. With $\mathcal{O}(10^2)$ confidently detected mergers in GWTC-4, features in this multidimensional parameter space are beginning to be resolved with enough granularity to begin addressing this question directly from the data, by asking which and how many subpopulations the data prefers.

Using a novel method to search for subpopulations within the BBH population leveraging RJ MCMC, we find evidence for three subpopulations with distinct mass, spin, and redshift: (i) a narrow concentration at $m_1 \approx 10 M_{\odot}$ with small positive χ_{eff} , a preference for unequal pairings, and the bulk of the merger rate, consistent with isolated field binary evolution including the SMT channel; (ii) a broad peak at $m_1 \sim 30 M_{\odot}$ with a χ_{eff} distribution centered on zero and a strong preference for

equal-mass pairings, consistent with dynamical assembly in dense stellar clusters; and (iii) a continuum extending from small to large masses with a positive-mean, broad χ_{eff} distribution, which contains the exceptional high-mass and high-spin events of the catalog but is inconsistent with originating exclusively from cluster hierarchical mergers, for which the χ_{eff} distribution should be symmetric about zero. The positive mean we recover hints at contributions from CHE or AGN-disk hierarchical mergers, and is plausibly explained by contributions from multiple channels.

We also find the first data-driven evidence for a faster evolution of the $10 M_{\odot}$ peak with redshift with respect to the $30 M_{\odot}$ peak, with the power-law rate index $\gamma_{10 M_{\odot}} > \gamma_{30 M_{\odot}}$ at 94.6% credibility in the most preferred model. Furthermore, the inferred value $\gamma_{10 M_{\odot}} = 5.7^{+2.1}_{-2.8}$ implies short delay-time distributions and inefficient BBH formation at metallicities above $Z_{\text{max}} \lesssim 0.1 Z_{\odot}$, assuming a Madau-Dickinson star formation history. Understanding the astrophysical implications of this result more rigorously will be an interesting next step for future work.

Previous works have identified subpopulations with distinct primary mass, mass ratio, and spin properties [34, 35]. For example, the 3-subpopulation mixture model of ref. [35] finds roughly the same three subpopulations as our analysis, with similar astrophysical interpretations. One significant difference, however, is that the χ_{eff} distribution of their broad continuum subpopulation is centered at 0 simply due to the fact that it was a targeted search for a hierarchical subpopulation, and thus the symmetry of the χ_{eff} distribution about 0 was enforced in the model prior. As this example illustrates, our framework has the advantage of being more agnostic than strongly-modeled analyses. Thus, we are able to verify their results and draw equally robust astrophysical conclusions with far more minimal prior assumptions, with the added benefit of not needing to manually compare the evidence for models of varying complexity. We also propose that moving forward, more flexible parametric distributions, such as the skew-t distribution, should be used to resolve features in the BBH population.

In conclusion, we demonstrate that it is possible to resolve robust, astrophysically-interpretable features in the BBH population without strong prior astrophysical assumptions imprinted in the model. Two of the three identified subpopulations map cleanly to an astrophysical formation channel, and the asymmetric spin signature of the high-spin continuum component is itself an informative result, and one that strongly parameterized analyses tailored to a hierarchical interpretation are not free to recover. Furthermore, our results can already confidently attribute most of the events in the catalog to a subpopulation, and therefore a possible formation channel. Upcoming catalogs will have source counts approaching $\mathcal{O}(10^3)$ [117] as well as better-measured source parameters, including the component spins. We expect that the inclusion of spin parameters beyond χ_{eff} , along with a larger catalog, will be able to resolve the high-spin continuum component into its constituent formation channels. It should also sharpen the constraints on the delay-time distribution and the metallicity dependence of BBH formation, and allow us to identify the formation channel of individual events with much higher confidence. The long-standing question of the origins of BBHs is, at last, becoming an empirical one.

6 Methodology

In this section, we explain the technical details of our methodology. We describe the basics of hierarchical Bayesian inference of GW data in Section 6.1, and the details of our population models in Section 6.2, including a population model in which we verify the existence of a secondary mass gap as found in ref. [94]. Then, we describe RJ MCMC in Section 6.3 and the implementation details in Section 6.4. In Section 6.5, we describe how we computed the population-weighted posteriors and subpopulation probabilities reported in Section 3. Finally, in Section 6.6 we describe our approach to sorting the identified subpopulations.

6.1 Hierarchical Bayesian inference

Given a catalog of observed BBHs, we are interested in inferring the population properties from which these BBHs arise. One can do this by means of hierarchical Bayesian inference. Recalling Eq. (1), given some population model $dN/d\boldsymbol{\theta}/dt$ governed by subpopulation parameters $\boldsymbol{\lambda}$ and global population parameters $\boldsymbol{\Lambda}$, one can infer the posterior distribution on $\boldsymbol{\lambda}, \boldsymbol{\Lambda}$ given the data. This inference is hierarchical because the population is informed by the observed distribution of source parameters $\boldsymbol{\theta} = [m_1, q, \chi_{\text{eff}}, z]$, which are in turn inferred from the GW strain data for each event via a Bayesian inference step called parameter estimation (PE). Therefore, one must marginalize over $\boldsymbol{\theta}$ for each event. The likelihood of N observed BBHs $\{d\}$ under selection effects is given by an inhomogeneous Poisson likelihood [118–120]

$$\mathcal{L}(\{d\} | \{\boldsymbol{\lambda}\}, \boldsymbol{\Lambda}) \propto e^{-\xi(\{\boldsymbol{\lambda}\}, \boldsymbol{\Lambda})N(\{\boldsymbol{\lambda}\}, \boldsymbol{\Lambda})} \prod_{i=1}^{N_{\text{obs}}} \int \frac{dN}{d\boldsymbol{\theta}}(\{\boldsymbol{\lambda}\}, \boldsymbol{\Lambda}) \frac{p_{\text{PE}}(\boldsymbol{\theta}|d_i)}{\pi_{\text{PE}}(\boldsymbol{\theta})} d\boldsymbol{\theta} \quad (3)$$

where $p_{\text{PE}}(\boldsymbol{\theta}|d_i)$ and $\pi_{\text{PE}}(\boldsymbol{\theta})$ are the PE posterior and prior, respectively, and thus we can evaluate Eq. (3) via Monte Carlo integration over the PE posterior samples. $\xi(\{\boldsymbol{\lambda}\}, \boldsymbol{\Lambda})$ is the expected fraction of events in the spacetime volume covered by the population prior and observing time that are detected. This is computed via Monte Carlo integration over an injection campaign of mock events [121–123].

The output of the Monte Carlo integration of a finite number of samples can deviate significantly from the true integral if the distribution of samples deviates significantly from the population distribution over which they are integrated [124, 125]. To limit this error, we impose a threshold on the variance of the Monte Carlo log-likelihood estimator $\sigma_{\text{ln } \mathcal{L}}^2$, which includes the errors from both the estimators of the individual event-level likelihoods and the selection function. Expressions for $\sigma_{\text{ln } \mathcal{L}}^2$ corresponding to Eq. (3) can be found in e.g. [121, 126]. During the inference, we set the likelihood to 0 in regions of parameter space where $\sigma_{\text{ln } \mathcal{L}}^2 \geq 1$, following [125].

6.2 Population models

The results of the inference will naturally depend on the parametric form that one chooses for each $dN_k/d\boldsymbol{\theta}$. In making this choice, one needs to strike a balance between imposing prior assumptions that are too strong (which could bias the results of the

inference) and prior assumptions that are too weak (which could lead to overfitting of the data as well as computational challenges). Thus, we implement several variants of population models, which we describe below. A list of all of our population parameters across all population models, as well as the priors used during the inference, can be found in Table 1.

Default model (skewt). Inspired by the common phenomenological modeling of the primary mass distribution as a mixture model of power-law and Gaussian distributions [33, 61], we model the primary mass distribution as a Jones and Faddy skew-t distribution [127], which has the property of being able to asymptotically approach both tail-heavy power-law behavior as well as Gaussian behavior. It is given by

$$\mathcal{S}(x; a, b) = C_{a,b}^{-1} \left(1 + \frac{x}{(a+b+x^2)^{1/2}} \right)^{a+1/2} \left(1 - \frac{x}{(a+b+x^2)^{1/2}} \right)^{b+1/2} \quad (4)$$

for real numbers $a > 0$ and $b > 0$, where $C_{a,b} = 2^{a+b-1} B(a, b) (a+b)^{1/2}$, and B is the beta function. The general skew-t distribution has power-law behavior $\propto |x|^{2a+1}$ as $x \rightarrow \infty$ and $\propto |x|^{2b+1}$ as $x \rightarrow -\infty$; setting $a = b = \nu/2$ recovers the Student-t distribution with ν degrees of freedom. Subsequently taking the limit $\nu \rightarrow \infty$ recovers a standard Gaussian distribution.

We allow for a shift parameter μ_m and a scale parameter σ_m , evaluating Eq. (4) at

$$x = \frac{m_1 - \mu_m}{\sigma_m}, \quad (5)$$

and truncate the distribution at a global m_{\min} as well as the maximum mass m_{\max} that we pin to $300 M_{\odot}$, following [33]. Finally, we re-parameterize and shift the distribution in Eq. (4) to improve the sampling efficiency. The final primary mass distribution we use is

$$p_{\mathcal{S}}(m_1 | \log \alpha, \log \kappa, \mu_m, \sigma_m, m_{\min}, m_{\max}) \propto \begin{cases} \frac{1}{\sigma_m} \mathcal{S} \left(\frac{m_1 - \mu_m}{\sigma_m} + \tilde{m}; \frac{\alpha \kappa}{1 + \kappa}, \frac{\alpha}{1 + \kappa} \right) & m_{\min} \leq m_1 \leq m_{\max} \\ 0 & \text{otherwise.} \end{cases} \quad (6)$$

where a, b have been re-parameterized to a tail weight parameter $\alpha = a + b$ and skew parameter $\kappa = a/b$, and \tilde{m} is the mode of Eq. (4), given by

$$\tilde{m}(a, b) = \frac{(a-b)\sqrt{a+b}}{\sqrt{(2a+1)(2b+1)}}. \quad (7)$$

With this parameterization, μ_m is the mode of the distribution, σ_m measures the width of the peak, κ characterizes the asymmetry of the power law tails, and α measures the tail weight, with large α approaching a Gaussian distribution.

We model the conditional mass ratio distribution as a truncated Gaussian with mean μ_q and width σ_q

$$p(q|m_1, \mu_q, \sigma_q, m_{\min}) = \mathcal{N}\left(q; \mu_q, \sigma_q, \frac{m_{\min}}{m_1}, 1\right), \quad (8)$$

which allows for a peak in $p(q|m_1)$ away from $q = 1$, motivated by possible formation mechanisms which favor unequal masses, including the SMT channel [72] and hierarchical mergers in AGN disks or clusters [11, 128, 129]. Here and henceforth, $\mathcal{N}(x; \mu, \sigma, x_{\min}, x_{\max})$ will denote a Gaussian with mean μ and standard deviation σ , truncated on $x \in [x_{\min}, x_{\max}]$.

Finally, we use for all models a truncated Gaussian for the χ_{eff} distribution, with mean μ_χ and width σ_χ

$$p(\chi_{\text{eff}}|\mu_\chi, \sigma_\chi) = \mathcal{N}(\chi_{\text{eff}}; \mu_\chi, \sigma_\chi, -1, 1). \quad (9)$$

Power-laws and peaks (NPLNP). In this model, a subpopulation's primary mass distribution is given by either a power-law distribution or a Gaussian. This allows us to compare our results more directly to phenomenological analyses in the literature. In this framework, the primary mass distribution is then a sum of n_{PL} power-laws and n_{G} Gaussians, where $1 \leq n_{\text{PL}}, n_{\text{G}} \leq 2$ [†].

Our implementation of a power-law distribution with low-mass tapering is slightly different from the standard form used by the LVK. Instead of a Planck tapering function, we use a power-law smoothing parameter p , making our probability distribution analytically normalizable:

$$p_{\text{PL}}(m_1|\alpha, p, m_{\min}^{\text{PL}}, m_{\min}, m_{\max}^{\text{PL}}) = \begin{cases} \frac{1}{C} m_1^{-\alpha} \left(1 - \frac{\tilde{m}_{\min}}{m_1}\right)^p & \tilde{m}_{\min} \leq m_1 \leq m_{\max}^{\text{PL}} \\ 0 & \text{otherwise.} \end{cases} \quad (10)$$

Here, $-\alpha$ is the usual power-law index, and each subpopulation is allowed its own m_{\min}^{PL} , and thus the distribution is smoothed to 0 at

$$\tilde{m}_{\min} = \max[m_{\min}, m_{\min}^{\text{PL}}]. \quad (11)$$

where m_{\min} is the global BBH minimum mass. Additionally, each subpopulation also has its own $m_{\max}^{\text{PL}} \leq m_{\max}$. This effectively allows for a broken power-law as a sum of two power-laws with non-overlapping bounds. As in the default model, the global m_{\max} is pinned at $300 M_\odot$.

The normalization of Eq. (10) is given by

$$C = (\tilde{m}_{\min})^{1-\alpha} I_{1-\tilde{m}_{\min}/m_{\max}^{\text{PL}}}(p+1, \alpha-1) \quad (12)$$

[†]In preliminary analyses we have found that more than 2 of either component is strongly disfavored, and thus for better convergence of our final result we limited the sampler to a maximum of 2 of each component.

where $I_u(a, b)$ is the incomplete beta function. Note that the normalization here is valid only for $\alpha > 1$; computing the normalization for $\alpha \leq 1$ involves hypergeometric functions, and thus for computational convenience, we exclude $\alpha \leq 1$ from the prior.

The Gaussian component is given by

$$p_{\mathcal{G}}(m_1 | \mu_q, \sigma_q, m_{\min}) = \mathcal{N}(m_1; \mu_m, \sigma_m, m_{\min}, m_{\max}), \quad (13)$$

and therefore the total BBH population distribution for n_{PL} power-law components and $n_{\mathcal{G}}$ Gaussian components is given by

$$\frac{dN}{d\theta}(\{\boldsymbol{\lambda}\}, \mathbf{\Lambda}) = T_{\text{obs}}(1+z)^{\gamma-1} \frac{dV_c}{dz} \left[\sum_{k=1}^{n_{\text{PL}}} \mathcal{R}_0^k p_{\text{PL}}(m_1 | \boldsymbol{\lambda}_{m, \text{PL}}^k, m_{\min}, m_{\max}) p(q | m_1, \boldsymbol{\lambda}_q^k, m_{\min}) p(\chi_{\text{eff}} | \boldsymbol{\lambda}_{\chi}^k) + \sum_{\ell=1}^{n_{\mathcal{G}}} \mathcal{R}_0^\ell p_{\mathcal{G}}(m_1 | \boldsymbol{\lambda}_{m, \mathcal{G}}^\ell, m_{\min}, m_{\max}) p(q | m_1, \boldsymbol{\lambda}_q^\ell, m_{\min}) p(\chi_{\text{eff}} | \boldsymbol{\lambda}_{\chi}^\ell) \right]. \quad (14)$$

where $\boldsymbol{\lambda}_\theta^k$ are the subpopulation parameters corresponding to distributions $p_k(\theta)$ given above, and $\mathbf{\Lambda} = [m_{\min}, \gamma]$ are global population parameters.

Identical mass distributions (skewt_ID). In general, it may be astrophysically more meaningful to model the distribution of *all* merging black holes, rather than the more massive one of the two in the binary, which can be obscured by both sorting uncertainties when the mass ratio is close to unity [130, 131] as well as astrophysical uncertainties (e.g., the primary mass of the BBH may not be the first born or the primary mass at zero age main sequence, due to mass ratio reversal [132, 133]). Thus, as an alternative, suppose both BBH masses are drawn from the same underlying distribution $m_A, m_B \sim f(m)$ with CDF $F(m)$, such that $m_1 = \max(m_A, m_B)$ and $m_2 = \min(m_A, m_B)$. Generically, we can write the joint probability distribution function as

$$p(m_1, m_2) = 2f(m_1)f(m_2)c(F(m_1), F(m_2)) \quad (15)$$

where c is a copula describing the pairing between the two masses. The factor of 2 accounts for the two possible orderings of (m_A, m_B) .

A simple choice for c is the bivariate Gaussian copula density with correlation parameter $\rho \in (-1, 1)$:

$$c(u, v; \rho) = \frac{1}{\sqrt{1-\rho^2}} \exp\left(\frac{2\rho z_1 z_2 - \rho^2(z_1^2 + z_2^2)}{2(1-\rho^2)}\right), \quad (16)$$

where $z_i = \Phi^{-1}(u_i)$, with Φ as the standard normal CDF (and Φ^{-1} its inverse). The marginal distributions for m_1 and m_2 can be shown to be

$$p(m_1 | \rho) = 2f(m_1) \Phi\left(\sqrt{\frac{1-\rho}{1+\rho}} \Phi^{-1}(F(m_1))\right) \quad (17)$$

$$p(m_2|\rho) = 2f(m_2) \Phi \left(-\sqrt{\frac{1-\rho}{1+\rho}} \Phi^{-1}(F(m_2)) \right). \quad (18)$$

We note that the marginals on the unordered masses, (m_A, m_B) are $(f(m_A), f(m_B))$ by the usual properties of a copula, but the marginals are modified when we take the max/min. For $\rho = 0$, the above expressions become $2f(m_1)F(m_1)$ and $2f(m_2)(1 - F(m_2))$, which are the usual pdfs of the max/min of independent-identically-distributed random variables. These expressions show how the correlation parameter ρ shifts the marginal distributions: positive ρ increases the probability of similar masses (both high or both low), while negative ρ favors dissimilar masses. At the extremes,

$$p(m_2 | m_1, \rho = 1) = \delta^D(m_2 - m_1) \quad (19)$$

$$p(m_2 | m_1, \rho = -1) = \delta^D(m_2 - F^{-1}(1 - F(m_1))) \quad (20)$$

where δ^D is the Dirac-delta function. For $\rho = 1$, the two masses are always equal, while at $\rho = -1$, m_2 is always at the quantile opposite of m_1 in the distribution $f(m)$.

Because copula models have the advantage of preserving the marginals of the two parameters, they have been used in past GW population analyses to search for correlations such as $q - \chi_{\text{eff}}$ [33, 114, 115], but not the pairing of BH masses. References [134, 135] analyzed the primary and secondary mass distributions of the BBH population, but with a power-law pairing function rather than a copula. This is therefore a novel population model that probes the underlying BH mass function of merging binaries and its binary pairings.

In the `skewt_ID` model, we model each subpopulation k as having its own correlation coefficient ρ_k and mass distribution $f_k(m) = p_S(m)$, which we model using the skew-t distribution given in Eq. (6).

Local redshift evolution (`skewt_z`). In this model, we relax the assumption of a global rate evolution and allow each subpopulation k to have its own power-law rate index γ_k ; it is otherwise identical to `skewt`.

Secondary mass maximum (`skewt_m2max`). Recently, [94] has found evidence for a gap in the secondary mass distribution, consistent with the theoretically predicted gap in the BH mass function from PISNe. We verify these results by employing a variant of our default population model in which the conditional mass ratio distribution is truncated at a secondary mass maximum $m_{2,\text{max}}$, which we infer as a global population parameter:

$$p(q|m_1, \mu_q, \sigma_q, m_{\text{min}}, m_{2,\text{max}}) = \mathcal{N} \left(q; \mu_q, \sigma_q, \frac{m_{\text{min}}}{m_1}, \min \left[1, \frac{m_{2,\text{max}}}{m_1} \right] \right). \quad (21)$$

This targets the steep drop-off of black holes in the secondary mass distribution beyond $\sim 45 M_\odot$ found by Tong et al. [94]. They find a gap in the secondary mass distribution, parameterizing the mass ratio distribution in a similar fashion to Eq. (21). Because the only event which populates the other side of the gap is GW231123, an analysis

which allows for a secondary mass maximum and excludes GW231123 should find a preference for a maximum consistent with the lower edge of the gap. Thus, we run `skewt_m2max` both including and excluding GW231123 from the analysis. We show the results for this analysis in Extended Data Fig. 1.

6.3 Reversible-jump MCMC

RJ MCMC [59] provides a powerful framework for exploring parameter spaces whose dimensionality is itself unknown. In addition to proposing updates to parameters within a given model, RJ MCMC allows transitions between models of different dimensionality by introducing or removing parameters. The update of parameters for a fixed dimensionality happens as in a regular MCMC. We now describe how updates to the number of components are performed.

As before, let $\{\boldsymbol{\lambda}\}_n = (\boldsymbol{\lambda}_1, \boldsymbol{\lambda}_2, \dots, \boldsymbol{\lambda}_n)$ be the hyperparameters of the n components of the model that are added or removed when adding or removing components, and $\boldsymbol{\Lambda}$ be the other hyperparameters. When proposing to add one component to a model with n components, the acceptance ratio is $\alpha = \min[1, H_{n \rightarrow n+1}]$ with Hastings ratio [136]

$$H_{n \rightarrow n+1} = \frac{p(\{d\}|\{\boldsymbol{\lambda}\}_{n+1}, \boldsymbol{\Lambda}) \pi(\{\boldsymbol{\lambda}\}_{n+1}) \pi(n+1)}{p(\{d\}|\{\boldsymbol{\lambda}\}_n, \boldsymbol{\Lambda}) \pi(\{\boldsymbol{\lambda}\}_n) \pi(n) q(\boldsymbol{\lambda}_{n+1})} \quad (22)$$

$$= \frac{p(\{d\}|\{\boldsymbol{\lambda}\}_{n+1}, \boldsymbol{\Lambda}) \pi(\boldsymbol{\lambda}_{n+1})}{p(\{d\}|\{\boldsymbol{\lambda}\}_n, \boldsymbol{\Lambda}) q(\boldsymbol{\lambda}_{n+1})} \quad (23)$$

where $\pi(\boldsymbol{\lambda})$ is the prior on $\boldsymbol{\lambda}$, $\pi(n)$ are the prior odds on a model with n components (which we take to be uniform across n), and $q(\boldsymbol{\lambda})$ is the distribution from which a new $\boldsymbol{\lambda}$ is proposed.

For a fixed proposal distribution $q(\boldsymbol{\lambda})$, a broader prior $\pi(\boldsymbol{\lambda})$ suppresses the second term in Eq. (23), implying that the newly proposed component must yield a larger increase in likelihood to be accepted. Conversely, proposals that are tightly concentrated in high-likelihood regions are penalized when they are much more localized than the prior. This behavior provides a direct implementation of Occam’s razor: models with additional components are only favored if they improve the fit to the data sufficiently to compensate for the increase in prior volume. In this work, we use the prior distribution itself as the proposal function, $q(\boldsymbol{\lambda}) = \pi(\boldsymbol{\lambda})$. In this case, the second term reduces to unity, but the Occam penalty is still present: as the prior volume increases, it becomes progressively harder to propose a new component that lands in a region of sufficiently high likelihood to be accepted. We find this choice to be a good compromise for our purpose. The acceptance ratio for removing a component is the inverse of Eq. (23), and the same considerations regarding the choice of prior and proposal apply.

RJ MCMC enables efficient Bayesian model selection: the ratio of samples corresponding to models with n_1 and n_2 components directly estimates the Bayes factor between these models.

6.4 Implementation and sampling details

We analyze the 153 BBHs in GWTC-4 [137] with False Alarm Rate $< 1 \text{ yr}^{-1}$, consistent with [32]. For events from O4a, we use PE samples [32] with the NRSur7dq4 waveform where available, and Mixed samples otherwise. For earlier events, we use PE samples [138] with the IMRPhenomXPHM waveform. For the RJ MCMC, we employ the implementation in `eryn` [139]. To improve computational efficiency, we have implemented our pipeline on GPUs; the analyses presented here require ≈ 10 hours for a 60,000 step run (including the burn-in) on a single GPU core.

The likelihood surface of a mixture model is highly degenerate, especially with respect to the rates of subpopulations: increasing the rate of one subpopulation naturally leads to a decrease in the rate of another subpopulation along level surfaces of the log-likelihood. Therefore, we implement two custom Gibbs proposal steps to traverse this likelihood surface, and use the default Gibbs Gaussian proposal for the remaining parameters.

The first custom move is an *orthogonal proposal* that updates the local merger rate vector $\mathcal{R} \equiv [\mathcal{R}_{0,1}, \mathcal{R}_{0,2}, \dots, \mathcal{R}_{0,n}]$ of the n subpopulations within the hyperplane orthogonal to $\mathbf{1}$, such that the total rate $\sum_k \mathcal{R}_{0,k}$ is conserved. Concretely, we draw $\Delta \sim \mathcal{N}(\mathbf{0}, \sigma_{\mathcal{R}}^2 \mathbf{1})$, where $\sigma_{\mathcal{R}}$ is a suitable proposal scale (which we take to be $\sigma_{\mathcal{R}} = 1 \text{ Gpc}^{-3} \text{ yr}^{-1}$), and perturb the walker by

$$\delta \mathcal{R} = \Delta - \text{mean}[\Delta], \quad (24)$$

where $\text{mean}[\mathbf{z}]$ is the mean of Δ over its n components.

Similarly, the second move is a *radial proposal* parallel to the $\mathbf{1}$ direction, with

$$\delta \mathcal{R} = \Delta \cdot \mathbf{1}, \quad \Delta \sim \mathcal{N}(0, \sigma_{\mathcal{R}}^2), \quad (25)$$

so that all rate components change by the same amount. This move changes the total rate without altering the relative rates between subpopulations. Alternating between these two Gibbs proposals therefore separates the redistribution of branching fraction among subpopulations from the overall rate normalization, improving mixing relative to a diagonal Gaussian proposal.

6.5 Population-weighted posteriors and probabilities

In Fig. 5, we showed the probabilities of subpopulation membership of various events in the catalog; in Figs. 4 and 7, we showed contours of their population-weighted posteriors, i.e. the posterior probability of the source parameters θ_i of event i given the data $\{d\}$. We derive expressions for these below.

Let $k = 1, 2, \dots, n$ index the subpopulations of a given model (of fixed dimensionality), and k_i denote the membership of event i to subpopulation k . From Bayes' theorem, the probability that event i belongs to subpopulation k conditioned on the data and population parameters $\{\lambda\}, \Lambda$ is given by

$$p(k_i|\{d\}) \propto \int d\{\lambda\} d\Lambda \mathcal{L}(d_i|k_i, \{\lambda\}, \Lambda) p(k_i|\{\lambda\}, \Lambda) p(\{\lambda\}, \Lambda|\{d\}_{\neq i}). \quad (26)$$

$p(\{\boldsymbol{\lambda}\}, \boldsymbol{\Lambda}|\{d\}_{\neq i})$ is the “leave-one-out” posterior probability of the hyperparameters that condition on the data of all events except for event i , to avoid double counting. This is related to the posterior probability of the full analysis via

$$p(\{\boldsymbol{\lambda}\}, \boldsymbol{\Lambda}|\{d\}_{\neq i}) \propto \frac{p(\{\boldsymbol{\lambda}\}, \boldsymbol{\Lambda}|\{d\})}{\mathcal{L}(d_i|\{\boldsymbol{\lambda}\}, \boldsymbol{\Lambda})} \quad (27)$$

taking advantage of the fact that the event-level likelihoods factorize. In Eq. (26), $p(k_i|\{\boldsymbol{\lambda}\}, \boldsymbol{\Lambda})$ is the probability of event i belonging to subpopulation k_i given the population; it has no dependence on $\{d\}_{\neq i}$ since it is conditionally independent of the other events’ data given the population parameters. It is given by

$$p(k_i|\{\boldsymbol{\lambda}\}, \boldsymbol{\Lambda}) = \frac{N_{k_i}(\boldsymbol{\lambda}_{k_i}, \boldsymbol{\Lambda})}{N(\{\boldsymbol{\lambda}\}, \boldsymbol{\Lambda})} \quad (28)$$

where $N_k(\boldsymbol{\lambda}_k, \boldsymbol{\Lambda})$ is the total expected number of mergers of subpopulation k , obtained by integrating its differential merger rate over $\boldsymbol{\theta}$.

The likelihood of d_i given that it belongs to subpopulation k_i and population parameters is

$$\mathcal{L}(d_i|k_i, \{\boldsymbol{\lambda}\}, \boldsymbol{\Lambda}) = \int d\boldsymbol{\theta} \frac{\mathcal{L}(d_i|\boldsymbol{\theta})}{N_{k_i}(\boldsymbol{\lambda}_{k_i}, \boldsymbol{\Lambda})} \frac{dN_{k_i}(\boldsymbol{\lambda}_{k_i}, \boldsymbol{\Lambda})}{d\boldsymbol{\theta}} \quad (29)$$

This can be approximated as a Monte Carlo sum over event i ’s posterior samples $\boldsymbol{\theta}_i^p$

$$\mathcal{L}(d_i|k_i, \{\boldsymbol{\lambda}\}, \boldsymbol{\Lambda}) \approx \sum_p \frac{1}{\pi_{\text{PE}}(\boldsymbol{\theta}_i^p)} \frac{1}{N_{k_i}(\boldsymbol{\lambda}_{k_i}, \boldsymbol{\Lambda})} \frac{dN_{k_i}(\boldsymbol{\lambda}_{k_i}, \boldsymbol{\Lambda})}{d\boldsymbol{\theta}} \quad (30)$$

Eq. (26) can finally be computed by multiplying together Eqs. (27), (28) and (30) and expressing the integral as a sum over population posterior samples $\{\boldsymbol{\lambda}^m\}, \boldsymbol{\Lambda}^m$

$$p(k_i|\{d\}) \approx \sum_p \frac{1}{\pi_{\text{PE}}(\boldsymbol{\theta}_i^p)} \sum_m \frac{dN_{k_i}(\boldsymbol{\lambda}_{k_i}^m, \boldsymbol{\Lambda}^m)}{d\boldsymbol{\theta}} \Big|_{\boldsymbol{\theta}_i^p} \left[N(\{\boldsymbol{\lambda}^m\}, \boldsymbol{\Lambda}^m) \mathcal{L}(d_i|\{\boldsymbol{\lambda}^m\}, \boldsymbol{\Lambda}^m) \right]^{-1} \quad (31)$$

which is what we used to compute the probabilities in Fig. 5. The bracketed quantities can be pre-computed for each population posterior sample m ; $\mathcal{L}(d_i|\{\boldsymbol{\lambda}^m\}, \boldsymbol{\Lambda}^m)$ can also be computed via Monte Carlo integration, marginalizing Eq. (29) over the different subpopulations

$$\mathcal{L}(d_i|\{\boldsymbol{\lambda}\}, \boldsymbol{\Lambda}) \approx \sum_p \frac{1}{\pi_{\text{PE}}(\boldsymbol{\theta}_i^p)} \frac{1}{N(\{\boldsymbol{\lambda}\}, \boldsymbol{\Lambda})} \sum_k \frac{dN_k(\boldsymbol{\lambda}_k, \boldsymbol{\Lambda})}{d\boldsymbol{\theta}} \quad (32)$$

Next, the population-weighted posterior

$$p(\boldsymbol{\theta}_i|\{d\}) \propto \mathcal{L}(d_i|\boldsymbol{\theta}_i) p(\boldsymbol{\theta}_i|\{d\}_{\neq i}) \quad (33)$$

can be obtained in a similar manner, following ref. [140]:

$$p(\boldsymbol{\theta}_i|\{d\}) \propto \frac{p(\boldsymbol{\theta}_i|d_i)}{\pi_{\text{PE}}(\boldsymbol{\theta}_i)} \sum_k \sum_m \frac{dN_k}{d\boldsymbol{\theta}}(\boldsymbol{\lambda}_k^m, \boldsymbol{\Lambda}^m) \Big|_{\boldsymbol{\theta}_i} \left[N(\{\boldsymbol{\lambda}^m\}, \boldsymbol{\Lambda}^m) \mathcal{L}(d_i|\{\boldsymbol{\lambda}^m\}, \boldsymbol{\Lambda}^m) \right]^{-1}. \quad (34)$$

In practice, we assign each posterior sample $\boldsymbol{\theta}_i^p$ a weight

$$w_i^p \propto \frac{1}{\pi_{\text{PE}}(\boldsymbol{\theta}_i^p)} \sum_k \sum_m \frac{dN_k}{d\boldsymbol{\theta}}(\boldsymbol{\lambda}_k, \boldsymbol{\Lambda}) \Big|_{\boldsymbol{\theta}_i^p} \left[N(\{\boldsymbol{\lambda}^m\}, \boldsymbol{\Lambda}^m) \mathcal{L}(d_i|\{\boldsymbol{\lambda}^m\}, \boldsymbol{\Lambda}^m) \right]^{-1} \quad (35)$$

from which we can use a kernel density estimator to create the contours in Figs. 4 and 7.

6.6 Subpopulation uniqueness

Because our goal is to search for distinct subpopulations in parameter space, one must penalize the sampler against fitting the data with multiple close-together or identical components when it can be fit with a single larger component. Furthermore, one also needs to be able to identify the different components found by the sampler in post-processing across all of the posterior samples. We do so by mapping for each subpopulation k the distribution $p_k(\theta|\boldsymbol{\lambda}_k, \boldsymbol{\Lambda})$ of each parameter θ to a whitened feature space \mathbf{x}_k roughly corresponding to the first two moments of the distribution. This mapping is used to ensure that found components are distinct during inference, as well as to sort components in post-processing into identified groups, or subpopulations.

We now describe this mapping $p \rightarrow \mathbf{x}$ as follows. For some BBH parameter $\theta \in [m_1, q, \chi_{\text{eff}}]$, each component k has its own probability distribution $p_k(\theta|\boldsymbol{\lambda}_k, \boldsymbol{\Lambda})$. We map this distribution into a feature space by computing a characteristic center $c_k^\theta(\boldsymbol{\lambda}_k, \boldsymbol{\Lambda})$ and width $w_k^\theta(\boldsymbol{\lambda}_k, \boldsymbol{\Lambda})$; we describe the formulae for these in Section 6.7. Because these quantities are in general dimensionful with different characteristic scales, we used the whitened vector

$$\mathbf{x}_k(\boldsymbol{\lambda}_k, \boldsymbol{\Lambda}) = \left[\frac{c_k^{m_1}}{\bar{m}}, \frac{w_k^{m_1}}{\bar{m}}, \frac{c_k^q}{\bar{q}}, \frac{w_k^q}{\bar{q}}, \frac{c_k^{\chi_{\text{eff}}}}{\bar{\chi}_{\text{eff}}}, \frac{w_k^{\chi_{\text{eff}}}}{\bar{\chi}_{\text{eff}}} \right], \quad (36)$$

rescaling each c_k^θ, w_k^θ by a characteristic whitening scale $\bar{\theta}$. Note that for $p_k(q)$, we are using the conditional mass ratio distribution in Eq. (8), except we take the truncation between 0 and 1 to remove the m_1 dependence for computational expediency. For the copula model `skewt_ID`, we compute the features of the total BBH mass distribution $f_k(m)$ rather than $p_k(m_1)$ and $p_k(q)$. For `skewt_z`, we add in the independent redshift evolution of each component by adding the redshift power-law index γ itself to the feature vector, similarly rescaled by a characteristic $\bar{\gamma}$.

In post-processing, a natural whitening scale $\bar{\theta}$ can be defined from both the standard deviation of the features used for clustering and the intrinsic standard deviation

of each component. Specifically, we define the whitening scales as

$$\bar{\theta} = \sqrt{\text{Var}[c^\theta] + \text{Var}[w^\theta] + \text{median}[w^\theta]^2} \quad \theta \in [m_1, q, \chi_{\text{eff}}] \quad (37)$$

$$\bar{\gamma} = \sqrt{\text{Var}[\gamma]}, \quad (38)$$

where sample median and variances are taken across the $c_k^\theta(\boldsymbol{\lambda}_k^m, \mathbf{\Lambda}^m)$, $w_k^\theta(\boldsymbol{\lambda}_k^m, \mathbf{\Lambda}^m)$, γ_k^m computed from the population draw corresponding to each posterior sample $\boldsymbol{\lambda}_k^m, \mathbf{\Lambda}^m$. This choice ensures that components are considered distinct only when their separation is larger than the corresponding statistical uncertainty and when the components themselves are sufficiently well separated to be distinguishable.

With the whitening scale computed with Eq. (37), we can now map each posterior sample output by the RJ MCMC to a feature vector as in Eq. (36), $p_k(\boldsymbol{\theta}|\boldsymbol{\lambda}_k^m, \mathbf{\Lambda}^m) \rightarrow \mathbf{x}_m^k$. We then sort the components by performing k -means clustering on these feature vectors, using the implementation in `scikit-learn` [141]. k -means clustering is a fast and simple clustering algorithm which finds clusters by initializing n_c cluster centroids and minimizing the distance between data points and their cluster centroids; because of this, whitening of the feature space is especially necessary. The number of centroids n_c must be provided by the user.

RJ MCMC returns posterior samples for all models being compared simultaneously, with the number of samples in each model proportional to the model evidences and therefore the Bayes factor. To identify corresponding subpopulations across different posterior samples, we apply the clustering algorithm to all inferred components within a given model family (e.g. power-laws, Gaussians or skew-ts), combining samples with different numbers of components n . In this way, components that appear in different posterior samples can be grouped into common clusters representing the same underlying subpopulation. Because the k -means algorithm requires the number of clusters, n_c , to be specified in advance, we set n_c equal to the largest number of components among all models that are not strongly disfavoured relative to the preferred model. Specifically, we consider all models with a Bayes factor $\mathcal{B} \geq 0.1$ with respect to the model with the highest evidence. The output of the clustering algorithm is what we use to identify subpopulations.

As discussed above, we also use Eq. (36) to enforce the uniqueness of components during inference. During the inference, we do not have access to the posterior distribution of c_k^θ, w_k^θ , needed to compute the whitening scale defined in Eq. 37, but, we still have a handle on the relevant scales of our different quantities. We use $\bar{m} = 8 M_\odot$, $\bar{q} = 0.3$, $\bar{\chi}_{\text{eff}} = 0.1$, and $\bar{\gamma} = 1.0$ to compute the $\{\mathbf{x}_k\}$ corresponding to the position of the walker. These values were chosen to match those of Eq. (37) in earlier test runs. We then enforce the separation of subpopulations by setting the likelihood to 0 when

$$\max [\text{abs}[\mathbf{x}_{k'} - \mathbf{x}_k]] < 1, \quad (39)$$

where the maximum is taken over the different vector elements. Thus, the likelihood is set to 0 when any two subpopulations are separated by less than 1 along all dimensions in the feature space of \mathbf{x} .

Although the results are not particularly sensitive to the exact choice of $\bar{\theta}$, ill-chosen $\bar{\theta}$ can cause in confusion in interpreting the results. For example, using a sufficiently small \bar{q} will cause poor sorting of subpopulations, since it effectively upweights the w^q, c^q dimensions of the feature space when the $p(q)$ are not particularly well constrained. Furthermore, $\bar{\theta}$ (and especially \bar{m}) that is too small allows the sampler to explore 3-component models consisting of two identical components, which should in principle be counted as a 2-component model. Although such cases are disfavored by the Occam’s razor penalty, their posterior support is small but non-negligible for $\bar{m} = 5 M_\odot$.

For population models with multiple model types, i.e., the NPLNP population model, there can still be confusion *between* model types. For example, in the most preferred “1 power-law + 2 Gaussians” model of NPLNP, both the $10 M_\odot$ feature and the $30 M_\odot$ feature are Gaussians in m_1 . However, both features can also be modeled with steep power-law distributions, and hence the “2 power-laws + 1 Gaussian” posterior is bimodal, with one power-law as the continuum, and the other power-law split between the $10 M_\odot$ and $30 M_\odot$ feature with about equal preference. Thus, upon comparing this result with Table 2, this means that both subpopulations prefer to be represented with a Gaussian with $\mathcal{B} \approx 3$.

6.7 Formulae for computing c and w

Truncated Gaussian, $\mathcal{N}(x; \mu, \sigma, x_{\min}, x_{\max})$.

$$c = \mu \tag{40}$$

$$w = \frac{F^{-1}(0.84; \mu, \sigma, x_{\min}, x_{\max}) - F^{-1}(0.16; \mu, \sigma, x_{\min}, x_{\max})}{2} \tag{41}$$

where F^{-1} is the inverse CDF of the truncated Gaussian. In terms of the standard normal CDF $\Phi(x)$, this is

$$\begin{aligned} F^{-1}(q) &= \mu + \sigma \Phi^{-1}[q_{\text{lo}} + q(q_{\text{hi}} - q_{\text{lo}})] \\ q_{\text{lo}} &= \Phi((x_{\min} - \mu)/\sigma) \\ q_{\text{hi}} &= \Phi((x_{\max} - \mu)/\sigma) \end{aligned} \tag{42}$$

The truncated Gaussian is used to model the conditional mass ratio distribution (where for simplicity c, w are evaluated at $x_{\min} = 0, x_{\max} = 1$) as well as the χ_{eff} distribution. It is also used to model m_1 in NPLNP.

Power-law with low-mass smoothing, $p_{\text{PL}}(m_1 | \alpha, p, m_{\min}^{\text{PL}}, m_{\max}^{\text{PL}})$. See Eq. (10).

$$c = x_{\min}(1 + p/\alpha) \tag{43}$$

$$w = \frac{1}{2} [F_{\text{PL}}^{-1}(0.5) - c] \tag{44}$$

where F_{PL}^{-1} is the inverse CDF for a truncated power-law distribution (ignoring the low-mass smoothing for simplicity)

$$F_{\text{PL}}^{-1}(q) = [(x_{\text{max}}^{1-\alpha} - x_{\text{min}}^{1-\alpha})q + x_{\text{min}}^{1-\alpha}]^{1/(1-\alpha)}. \quad (45)$$

This is also used for m_1 in NPLNP.

Jones and Faddy skew-t distribution, $p_{\mathcal{S}}(m_1 | \log \alpha, \log \kappa, \mu_m, \sigma_m, m_{\text{min}}, m_{\text{max}})$. See Eq. (6).

$$c = \mu \quad (46)$$

$$w = \sigma_m \left[\frac{(a+b)(a+b+1)^4}{(4ab+2(a+b)+1)^3} \right]^{1/2} \left[\frac{a+1/2}{(2a+1)^2} + \frac{b+1/2}{(2b+1)^2} \right]^{-1/2} \quad (47)$$

This is used for m_1 in all models except NPLNP.

Data Availability. All software used for this work is made available on Github ‡. The data underlying this article can be downloaded at ref. [142].

Acknowledgements. We are thankful to T. Bruel, H. Quelquejay-Leclere, Daniel Holz, and Colm Talbot for their constructive comments and to Hui Tong for completing the internal LVK review. A.Q.C. is currently supported by the Lowell Wood Endowed Fellowship of the Fannie and John Hertz foundation. A.T. is supported by MUR Young Researchers Grant No. SOE2024-0000125, ERC Starting Grant No. 945155–GWmining, Cariplo Foundation Grant No. 2021-0555, MUR PRIN Grant No. 2022-Z9X4XS, Italian-French University (UIF/UFI) Grant No. 2025-C3-386, MUR Grant “Progetto Dipartimenti di Eccellenza 2023-2027” (BiCoQ), and the ICSC National Research Centre funded by NextGenerationEU. This material is based upon work supported by NSF’s LIGO Laboratory which is a major facility fully funded by the National Science Foundation. The computational work for this manuscript was carried out on the compute clusters Saraswati and Hypatia at the Max Planck Institute for Gravitational Physics in Potsdam.

Competing interests. The authors declare that they have no competing financial interests.

References

- [1] Tutukov, A.V., Yungelson, L.R.: The merger rate of neutron star and black hole binaries. *Monthly Notices of the Royal Astronomical Society* **260**, 675–678 (1993) <https://doi.org/10.1093/mnras/260.3.675>
- [2] Kalogera, V.: Spin-Orbit Misalignment in Close Binaries with Two Compact Objects. *The Astrophysical Journal* **541**, 319–328 (2000) <https://doi.org/10.1086/309400>

‡<https://github.com/aqcheng/RJpop>

- [3] Grandclément, P., Ihm, M., Kalogera, V., Belczynski, K.: Searching for gravitational waves from the inspiral of precessing binary systems: Astrophysical expectations and detection efficiency of “spiky” templates. *Physical Review D* **69**, 102002 (2004) <https://doi.org/10.1103/PhysRevD.69.102002>
- [4] Postnov, K.A., Yungelson, L.R.: The Evolution of Compact Binary Star Systems. *Living Reviews in Relativity* **17**, 3 (2014) <https://doi.org/10.12942/lrr-2014-3>
- [5] Belczynski, K., Holz, D.E., Bulik, T., O’Shaughnessy, R.: The first gravitational-wave source from the isolated evolution of two stars in the 40-100 solar mass range. *Nature* **534**, 512–515 (2016) <https://doi.org/10.1038/nature18322>
- [6] Mandel, I., de Mink, S.E.: Merging binary black holes formed through chemically homogeneous evolution in short-period stellar binaries. *Monthly Notices of the Royal Astronomical Society* **458**, 2634–2647 (2016) <https://doi.org/10.1093/mnras/stw379>
- [7] Marchant, P., Langer, N., Podsiadlowski, P., Tauris, T.M., Moriya, T.J.: A new route towards merging massive black holes. *Astronomy and Astrophysics* **588**, 50 (2016) <https://doi.org/10.1051/0004-6361/201628133>
- [8] Rodriguez, C.L., Zevin, M., Pankow, C., Kalogera, V., Rasio, F.A.: Illuminating Black Hole Binary Formation Channels with Spins in Advanced LIGO. *The Astrophysical Journal* **832**, 2 (2016) <https://doi.org/10.3847/2041-8205/832/1/L2>
- [9] Stevenson, S., Vigna-Gómez, A., Mandel, I., Barrett, J.W., Neijssel, C.J., *et al.*, : Formation of the first three gravitational-wave observations through isolated binary evolution. *Nature Communications* **8**, 14906 (2017) <https://doi.org/10.1038/ncomms14906>
- [10] McKernan, B., Ford, K.E.S., Bellovary, J., Leigh, N.W.C., Haiman, Z., *et al.*, : Constraining Stellar-mass Black Hole Mergers in AGN Disks Detectable with LIGO. *The Astrophysical Journal* **866**, 66 (2018) <https://doi.org/10.3847/1538-4357/aadae5>
- [11] Yang, Y., Bartos, I., Gayathri, V., Ford, K.E.S., Haiman, Z., *et al.*, : Hierarchical Black Hole Mergers in Active Galactic Nuclei. *Physical Review Letters* **123**, 181101 (2019) <https://doi.org/10.1103/PhysRevLett.123.181101>
- [12] Tagawa, H., Haiman, Z., Bartos, I., Kocsis, B.: Spin Evolution of Stellar-mass Black Hole Binaries in Active Galactic Nuclei. *The Astrophysical Journal* **899**, 26 (2020) <https://doi.org/10.3847/1538-4357/aba2cc>
- [13] McKernan, B., Ford, K.E.S., O’Shaughnessy, R., Wysocki, D.: Monte Carlo simulations of black hole mergers in AGN discs: Low χ_{eff} mergers and predictions for LIGO. *Monthly Notices of the Royal Astronomical Society* **494**, 1203–1216

- (2020) <https://doi.org/10.1093/mnras/staa740>
- [14] Vaccaro, M.P., Mapelli, M., Périgois, C., Barone, D., Artale, M.C., *et al.*, : Impact of gas hardening on the population properties of hierarchical black hole mergers in active galactic nucleus disks. *Astronomy and Astrophysics* **685**, 51 (2024) <https://doi.org/10.1051/0004-6361/202348509>
- [15] Sigurdsson, S., Hernquist, L.: Primordial black holes in globular clusters. *Nature* **364**, 423–425 (1993) <https://doi.org/10.1038/364423a0>
- [16] Miller, M.C., Lauburg, V.M.: Mergers of Stellar-Mass Black Holes in Nuclear Star Clusters. *The Astrophysical Journal* **692**, 917–923 (2009) <https://doi.org/10.1088/0004-637X/692/1/917>
- [17] Portegies Zwart, S.F., McMillan, S.L.W., Gieles, M.: Young Massive Star Clusters. *Annual Review of Astronomy and Astrophysics* **48**, 431–493 (2010) <https://doi.org/10.1146/annurev-astro-081309-130834>
- [18] Benacquista, M.J., Downing, J.M.B.: Relativistic Binaries in Globular Clusters. *Living Reviews in Relativity* **16**, 4 (2013) <https://doi.org/10.12942/lrr-2013-4>
- [19] Liu, B., Lai, D.: Black Hole and Neutron Star Binary Mergers in Triple Systems: Merger Fraction and Spin-Orbit Misalignment. *The Astrophysical Journal* **863**, 68 (2018) <https://doi.org/10.3847/1538-4357/aad09f>
- [20] Antonini, F., Rodriguez, C.L., Petrovich, C., Fischer, C.L.: Precessional dynamics of black hole triples: Binary mergers with near-zero effective spin. *Monthly Notices of the Royal Astronomical Society* **480**, 58–62 (2018) <https://doi.org/10.1093/mnras/sly126>
- [21] Rodriguez, C.L., Antonini, F.: A Triple Origin for the Heavy and Low-spin Binary Black Holes Detected by LIGO/VIRGO. *The Astrophysical Journal* **863**, 7 (2018) <https://doi.org/10.3847/1538-4357/aacea4>
- [22] Yu, H., Ma, S., Giesler, M., Chen, Y.: Spin and eccentricity evolution in triple systems: From the Lidov-Kozai interaction to the final merger of the inner binary. *Physical Review D* **102**, 123009 (2020) <https://doi.org/10.1103/PhysRevD.102.123009>
- [23] Mandel, I., Broekgaarden, F.S.: Rates of compact object coalescences. *Living Reviews in Relativity* **25**, 1 (2022) <https://doi.org/10.1007/s41114-021-00034-3>
- [24] Breivik, K.: Population Synthesis of Gravitational Wave Sources. arXiv (2025). <https://doi.org/10.48550/arXiv.2502.03523>
- [25] Mandel, I., Farmer, A.: Merging stellar-mass binary black holes. *Physics Reports* **955**, 1–24 (2022) <https://doi.org/10.1016/j.physrep.2022.01.003>

- [26] Mapelli, M.: Formation Channels of Single and Binary Stellar-Mass Black Holes. In: Handbook of Gravitational Wave Astronomy, p. 16 (2021). https://doi.org/10.1007/978-981-15-4702-7_16-1
- [27] LIGO Scientific Collaboration, Aasi, J., Abbott, B.P., Abbott, R., Abbott, T., *et al.*, : Advanced LIGO. Classical and Quantum Gravity **32**, 074001 (2015) <https://doi.org/10.1088/0264-9381/32/7/074001>
- [28] Capote, E., Jia, W., Aritomi, N., Nakano, M., Xu, V., *et al.*, : Advanced LIGO detector performance in the fourth observing run. Physical Review D **111**, 062002 (2025) <https://doi.org/10.1103/PhysRevD.111.062002>
- [29] Soni, S., Berger, B.K., Davis, D., Di Renzo, F., Effler, A., *et al.*, : LIGO Detector Characterization in the first half of the fourth Observing run. Classical and Quantum Gravity **42**, 085016 (2025) <https://doi.org/10.1088/1361-6382/adc4b6>
- [30] Acernese, F., Agathos, M., Agatsuma, K., Aisa, D., Allemandou, N., *et al.*, : Advanced Virgo: A second-generation interferometric gravitational wave detector. Classical and Quantum Gravity **32**, 024001 (2015) <https://doi.org/10.1088/0264-9381/32/2/024001>
- [31] Akutsu, T., Ando, M., Arai, K., Arai, Y., Araki, S., *et al.*, : Overview of KAGRA: Detector design and construction history. Progress of Theoretical and Experimental Physics **2021**, 05–101 (2021) <https://doi.org/10.1093/ptep/ptaa125>
- [32] LIGO Scientific Collaboration, Virgo Collaboration, KAGRA: GWTC-4.0: Parameter Estimation Data Release. Zenodo (2025). <https://doi.org/10.5281/zenodo.16053484>
- [33] The LIGO Scientific Collaboration, the Virgo Collaboration, the KAGRA Collaboration, Abac, A.G., Abouelfettouh, I., *et al.*, : GWTC-4.0: Population Properties of Merging Compact Binaries. arXiv (2025). <https://doi.org/10.48550/arXiv.2508.18083>
- [34] Banagiri, S., Thrane, E., Lasky, P.D.: Evidence for Three Subpopulations of Merging Binary Black Holes at Different Primary Masses (2025). <https://doi.org/10.48550/arXiv.2509.15646>
- [35] Ray, A., Mukherjee, S., Zevin, M., Kalogera, V.: On the Astrophysical Origin of Binary Black Hole Subpopulations: A Tale of Three Channels? arXiv (2026). <https://doi.org/10.48550/arXiv.2603.17987>
- [36] Sridhar, O., Ray, A., Kalogera, V.: Characterizing Binary Black Hole Subpopulations in GWTC-4 with Binned Gaussian Processes: On the Origins of the $35M_{\odot}$ Peak. arXiv (2025). <https://doi.org/10.48550/arXiv.2511.22093>

- [37] Plunkett, C., Callister, T., Zevin, M., Vitale, S.: Signatures of a Subpopulation of Hierarchical Mergers in the GWTC-4 Gravitational-Wave Dataset. arXiv (2026). <https://doi.org/10.48550/arXiv.2601.07908>
- [38] Zevin, M., Bavera, S.S., Berry, C.P.L., Kalogera, V., Fragos, T., *et al.*, : One Channel to Rule Them All? Constraining the Origins of Binary Black Holes Using Multiple Formation Pathways. *The Astrophysical Journal* **910**, 152 (2021) <https://doi.org/10.3847/1538-4357/abe40e>
- [39] Kimball, C., Talbot, C., Berry, C.P.L., Zevin, M., Thrane, E., *et al.*, : Evidence for Hierarchical Black Hole Mergers in the Second LIGO-Virgo Gravitational Wave Catalog. *The Astrophysical Journal* **915**, 35 (2021) <https://doi.org/10.3847/2041-8213/ac0aef>
- [40] Wang, Y.-Z., Li, Y.-J., Vink, J.S., Fan, Y.-Z., Tang, S.-P., *et al.*, : Potential Subpopulations and Assembling Tendency of the Merging Black Holes. *The Astrophysical Journal* **941**, 39 (2022) <https://doi.org/10.3847/2041-8213/aca89f>
- [41] Li, Y.-J., Wang, Y.-Z., Tang, S.-P., Fan, Y.-Z.: Resolving the Stellar-Collapse and Hierarchical-Merger Origins of the Coalescing Black Holes. *Physical Review Letters* **133**, 051401 (2024) <https://doi.org/10.1103/PhysRevLett.133.051401>
- [42] Pierra, G., Mastrogiovanni, S., Perriès, S.: The spin magnitude of stellar-mass black holes evolves with the mass. *Astronomy and Astrophysics* **692**, 80 (2024) <https://doi.org/10.1051/0004-6361/202452545>
- [43] Tong, H., Callister, T.A., Fishbach, M., Thrane, E., Antonini, F., *et al.*, : A Subpopulation of Low-Mass, Spinning Black Holes: Signatures of Dynamical Assembly. arXiv (2025). <https://doi.org/10.48550/arXiv.2511.05316>
- [44] Li, Y.-J., Wang, Y.-Z., Tang, S.-P., Fan, Y.-Z.: Aligned Hierarchical Black Hole Mergers in AGN Disks Revealed by GWTC-4. arXiv (2025). <https://doi.org/10.48550/arXiv.2509.23897>
- [45] Colloms, S., Berry, C.P.L., Veitch, J., Zevin, M.: Exploring the Evolution of Gravitational-wave Emitters with Efficient Emulation: Constraining the Origins of Binary Black Holes Using Normalizing Flows. *The Astrophysical Journal* **988**, 189 (2025) <https://doi.org/10.3847/1538-4357/ade546>
- [46] Wong, K.W.K., Breivik, K., Farr, W.M., Luger, R.: Backward Population Synthesis: Mapping the Evolutionary History of Gravitational-wave Progenitors. *The Astrophysical Journal* **950**, 181 (2023) <https://doi.org/10.3847/1538-4357/acc863>
- [47] Cheng, A.Q., Zevin, M., Vitale, S.: What You Don't Know Can Hurt You: Use and Abuse of Astrophysical Models in Gravitational-wave Population Analyses.

The Astrophysical Journal **955**, 127 (2023) <https://doi.org/10.3847/1538-4357/aced98>

- [48] Callister, T.A., Farr, W.M.: Parameter-Free Tour of the Binary Black Hole Population. *Physical Review X* **14**, 021005 (2024) <https://doi.org/10.1103/PhysRevX.14.021005>
- [49] Edelman, B., Farr, B., Doctor, Z.: Cover Your Basis: Comprehensive Data-driven Characterization of the Binary Black Hole Population. *The Astrophysical Journal* **946**, 16 (2023) <https://doi.org/10.3847/1538-4357/acb5ed>
- [50] Ray, A., Hernandez, I.M., Mohite, S., Creighton, J., Kapadia, S.: Nonparametric Inference of the Population of Compact Binaries from Gravitational-wave Observations Using Binned Gaussian Processes. *The Astrophysical Journal* **957**, 37 (2023) <https://doi.org/10.3847/1538-4357/acf452>
- [51] Tiwari, V.: VAMANA: Modeling binary black hole population with minimal assumptions. *Classical and Quantum Gravity* **38**, 155007 (2021) <https://doi.org/10.1088/1361-6382/ac0b54>
- [52] Heinzl, J., Mould, M., Álvarez-López, S., Vitale, S.: High resolution non-parametric inference of gravitational-wave populations in multiple dimensions. *Physical Review D* **111**, 063043 (2025) <https://doi.org/10.1103/PhysRevD.111.063043>
- [53] Rinaldi, S., Del Pozzo, W.: (H)DPGMM: A hierarchy of Dirichlet process Gaussian mixture models for the inference of the black hole mass function. *Monthly Notices of the Royal Astronomical Society* **509**, 5454–5466 (2022) <https://doi.org/10.1093/mnras/stab3224>
- [54] Toubiana, A., Katz, M.L., Gair, J.R.: Is there an excess of black holes around 20 M_{\odot} ? Optimizing the complexity of population models with the use of reversible jump MCMC. *Monthly Notices of the Royal Astronomical Society* **524**, 5844–5853 (2023) <https://doi.org/10.1093/mnras/stad2215>
- [55] Payne, E., Thrane, E.: Model exploration in gravitational-wave astronomy with the maximum population likelihood. *Physical Review Research* **5**, 023013 (2023) <https://doi.org/10.1103/PhysRevResearch.5.023013>
- [56] Afroz, S., Mukherjee, S.: Binary Black Hole Phase Space Discovers the Signature of Pair Instability Supernovae Mass Gap. *arXiv* (2025). <https://doi.org/10.48550/arXiv.2509.09123>
- [57] Alvarez-Lopez, S., Heinzl, J., Mould, M., Vitale, S.: Nowhere Left to Hide: Revealing Realistic Gravitational-Wave Populations in High Dimensions and High Resolution with PixelPop. *arXiv* (2025). <https://doi.org/10.48550/arXiv.2506.20731>

- [58] Gennari, V., Bertheas, T., Tamanini, N.: Emergent Structure in the Binary Black Hole Mass Distribution and Implications for Population-Based Cosmology. arXiv (2026). <https://doi.org/10.48550/arXiv.2604.14290>
- [59] Green, P.J.: Reversible jump Markov chain Monte Carlo computation and Bayesian model determination. *Biometrics* **82**, 711–732 (1995) <https://doi.org/10.1093/biomet/82.4.711>
- [60] Tenorio, R., Toubiana, A., Bruel, T., Gerosa, D., Gair, J.R.: Where did Heavy Binaries Go? Gravitational-wave Populations Using Delaunay Triangulation with Optimized Complexity. *The Astrophysical Journal* **994**, 52 (2025) <https://doi.org/10.3847/2041-8213/ae1cbd>
- [61] Talbot, C., Thrane, E.: Measuring the Binary Black Hole Mass Spectrum with an Astrophysically Motivated Parameterization. *The Astrophysical Journal* **856**, 173 (2018) <https://doi.org/10.3847/1538-4357/aab34c>
- [62] Banagiri, S., Callister, T.A., Adamcewicz, C., Doctor, Z., Kalogera, V.: Structure and Skewness of the Effective Inspiral Spin Distribution of Binary Black Hole Mergers. *The Astrophysical Journal* **990**, 147 (2025) <https://doi.org/10.3847/1538-4357/adf4c6>
- [63] Bavera, S.S., Fragos, T., Qin, Y., Zapartas, E., Neijssel, C.J., *et al.*, : The origin of spin in binary black holes. Predicting the distributions of the main observables of Advanced LIGO. *Astronomy and Astrophysics* **635**, 97 (2020) <https://doi.org/10.1051/0004-6361/201936204>
- [64] Qin, Y., Fragos, T., Meynet, G., Andrews, J., Sørensen, M., *et al.*: The spin of the second-born black hole in coalescing binary black holes. *Astronomy and Astrophysics* **616**, 28 (2018) <https://doi.org/10.1051/0004-6361/201832839>
- [65] Ma, L., Fuller, J.: Tidal Spin-up of Black Hole Progenitor Stars. *The Astrophysical Journal* **952**, 53 (2023) <https://doi.org/10.3847/1538-4357/acdb74>
- [66] Fuller, J., Ma, L.: Most Black Holes Are Born Very Slowly Rotating. *The Astrophysical Journal* **881**, 1 (2019) <https://doi.org/10.3847/2041-8213/ab339b>
- [67] Tiwari, V., Fairhurst, S.: The Emergence of Structure in the Binary Black Hole Mass Distribution. *The Astrophysical Journal* **913**, 19 (2021) <https://doi.org/10.3847/2041-8213/abfbe7>
- [68] Abbott, R., Abbott, T.D., Acernese, F., Ackley, K., Adams, C., *et al.*, : Population of Merging Compact Binaries Inferred Using Gravitational Waves through GWTC-3. *Physical Review X* **13**, 011048 (2023) <https://doi.org/10.1103/PhysRevX.13.011048>
- [69] Legred, I., Golomb, J., Chatziioannou, K.: Low-Mass Failed Supernovae and

- the $10^{-10} M_{\odot}$ Peak in the Merging Black Hole Mass Distribution. arXiv (2026). <https://doi.org/10.48550/arXiv.2604.01420>
- [70] van Son, L.A.C., de Mink, S.E., Renzo, M., Justham, S., Zapartas, E., *et al.*, : No Peaks without Valleys: The Stable Mass Transfer Channel for Gravitational-wave Sources in Light of the Neutron Star-Black Hole Mass Gap. *The Astrophysical Journal* **940**, 184 (2022) <https://doi.org/10.3847/1538-4357/ac9b0a>
- [71] van Son, L.A.C., de Mink, S.E., Chruślińska, M., Conroy, C., Pakmor, R., *et al.*: The Locations of Features in the Mass Distribution of Merging Binary Black Holes Are Robust against Uncertainties in the Metallicity-dependent Cosmic Star Formation History. *The Astrophysical Journal* **948**, 105 (2023) <https://doi.org/10.3847/1538-4357/acbf51>
- [72] Olejak, A., Klencki, J., Xu, X.-T., Wang, C., Belczynski, K., *et al.*: Unequal-mass highly spinning binary black hole mergers in the stable mass transfer formation channel. *Astronomy and Astrophysics* **689**, 305 (2024) <https://doi.org/10.1051/0004-6361/202450480>
- [73] Neijssel, C.J., Vigna-Gómez, A., Stevenson, S., Barrett, J.W., Gaebel, S.M., *et al.*, : The effect of the metallicity-specific star formation history on double compact object mergers. *Monthly Notices of the Royal Astronomical Society* **490**, 3740–3759 (2019) <https://doi.org/10.1093/mnras/stz2840>
- [74] van Son, L.A.C., de Mink, S.E., Callister, T., Justham, S., Renzo, M., *et al.*, : The Redshift Evolution of the Binary Black Hole Merger Rate: A Weighty Matter. *The Astrophysical Journal* **931**, 17 (2022) <https://doi.org/10.3847/1538-4357/ac64a3>
- [75] Galaudage, S., Lamberts, A.: Compactness peaks: An astrophysical interpretation of the mass distribution of merging binary black holes. *Astronomy and Astrophysics* **694**, 186 (2025) <https://doi.org/10.1051/0004-6361/202451654>
- [76] Schneider, F.R.N., Podsiadlowski, P., Laplace, E.: Bimodal Black Hole Mass Distribution and Chirp Masses of Binary Black Hole Mergers. *The Astrophysical Journal* **950**, 9 (2023) <https://doi.org/10.3847/2041-8213/acd77a>
- [77] Willcox, R., Schneider, F.R.N., Laplace, E., Podsiadlowski, P., Maltsev, K., *et al.*, : Good Things Always Come in 3s: Trimodality in the Binary Black-Hole Chirp-Mass Distribution Supports Bimodal Black-Hole Formation. arXiv (2025). <https://doi.org/10.48550/arXiv.2510.07573>
- [78] Burrows, A., Wang, T., Vartanyan, D.: Physical Correlations and Predictions Emerging from Modern Core-collapse Supernova Theory. *The Astrophysical Journal* **964**, 16 (2024) <https://doi.org/10.3847/2041-8213/ad319e>
- [79] Gerosa, D., Fishbach, M.: Hierarchical mergers of stellar-mass black holes and

- their gravitational-wave signatures. *Nature Astronomy* **5**, 749–760 (2021) <https://doi.org/10.1038/s41550-021-01398-w>
- [80] Rodriguez, C.L., Haster, C.-J., Chatterjee, S., Kalogera, V., Rasio, F.A.: Dynamical Formation of the GW150914 Binary Black Hole. *The Astrophysical Journal* **824**, 8 (2016) <https://doi.org/10.3847/2041-8205/824/1/L8>
- [81] Park, D., Kim, C., Lee, H.M., Bae, Y.-B., Belczynski, K.: Black hole binaries dynamically formed in globular clusters. *Monthly Notices of the Royal Astronomical Society* **469**, 4665–4674 (2017) <https://doi.org/10.1093/mnras/stx1015>
- [82] Antonini, F., Gieles, M., Dosopoulou, F., Chattopadhyay, D.: Coalescing black hole binaries from globular clusters: Mass distributions and comparison to gravitational wave data from GWTC-3. *Monthly Notices of the Royal Astronomical Society* **522**, 466–476 (2023) <https://doi.org/10.1093/mnras/stad972>
- [83] Bruel, T., Lamberts, A., Rodriguez, C.L., Feldmann, R., Grudić, M.Y., *et al.*: Great Balls of FIRE: IV. Contribution of massive star clusters to the astrophysical population of merging binary black holes. *Astronomy and Astrophysics* **701**, 252 (2025) <https://doi.org/10.1051/0004-6361/202554454>
- [84] Arca Sedda, M., Paiella, L., Ugolini, C., Santoliquido, F., Mestichelli, B., *et al.*: Isolated or Dynamical? Tracing Black Hole Binary Formation through the Population of Gravitational-Wave Sources. *arXiv* (2026). <https://doi.org/10.48550/arXiv.2603.20430>
- [85] Cook, H.E., McKernan, B., Ford, K.E.S., Delfavero, V., Nathaniel, K., *et al.*: McFACTS. II. Mass Ratio-Effective Spin Relationship of Black Hole Mergers in the Active Galactic Nucleus Channel. *The Astrophysical Journal* **993**, 163 (2025) <https://doi.org/10.3847/1538-4357/adfd56>
- [86] Abbott, B.P., Abbott, R., Abbott, T.D., Abraham, S., Acernese, F., *et al.*: Binary Black Hole Population Properties Inferred from the First and Second Observing Runs of Advanced LIGO and Advanced Virgo. *The Astrophysical Journal* **882**, 24 (2019) <https://doi.org/10.3847/2041-8213/ab3800>
- [87] Rodriguez, C.L., Zevin, M., Amaro-Seoane, P., Chatterjee, S., Kremer, K., *et al.*: Black holes: The next generation—repeated mergers in dense star clusters and their gravitational-wave properties. *Physical Review D* **100**, 043027 (2019) <https://doi.org/10.1103/PhysRevD.100.043027>
- [88] Antonini, F., Romero-Shaw, I.M., Callister, T.: Star Cluster Population of High Mass Black Hole Mergers in Gravitational Wave Data. *Physical Review Letters* **134**, 011401 (2025) <https://doi.org/10.1103/PhysRevLett.134.011401>
- [89] Antonini, F., Romero-Shaw, I., Callister, T., Dosopoulou, F., Chattopadhyay, D.,

- et al.*, : Gravitational Waves Reveal the Pair-Instability Mass Gap and Constrain Nuclear Burning in Massive Stars (2025). <https://doi.org/10.48550/arXiv.2509.04637>
- [90] de Mink, S.E., Mandel, I.: The chemically homogeneous evolutionary channel for binary black hole mergers: Rates and properties of gravitational-wave events detectable by advanced LIGO. *Monthly Notices of the Royal Astronomical Society* **460**, 3545–3553 (2016) <https://doi.org/10.1093/mnras/stw1219>
- [91] Popa, S.A., de Mink, S.E.: Very Massive, Rapidly Spinning Binary Black Hole Progenitors through Chemically Homogeneous Evolution—The Case of GW231123. *The Astrophysical Journal* **995**, 76 (2025) <https://doi.org/10.3847/2041-8213/ae20f1>
- [92] Bartos, I., Kocsis, B., Haiman, Z., Márka, S.: Rapid and Bright Stellar-mass Binary Black Hole Mergers in Active Galactic Nuclei. *The Astrophysical Journal* **835**, 165 (2017) <https://doi.org/10.3847/1538-4357/835/2/165>
- [93] Delfavero, V., Ford, K.E.S., McKernan, B., Cook, H.E., Nathaniel, K., *et al.*, : McFACTS III: Compact Binary Mergers from Active Galactic Nucleus Disks over an Entire Synthetic Universe. *The Astrophysical Journal* **989**, 67 (2025) <https://doi.org/10.3847/1538-4357/ade4c1>
- [94] Tong, H., Fishbach, M., Thrane, E., Mould, M., Callister, T.A., *et al.*, : Evidence of the Pair Instability Gap in the Distribution of Black Hole Masses. *arXiv* (2025). <https://doi.org/10.48550/arXiv.2509.04151>
- [95] Abbott, R., Abbott, T.D., Abraham, S., Acernese, F., Ackley, K., *et al.*, : GW190412: Observation of a binary-black-hole coalescence with asymmetric masses. *Physical Review D* **102**, 043015 (2020) <https://doi.org/10.1103/PhysRevD.102.043015>
- [96] Abac, A.G., Abouelfettouh, I., Acernese, F., Ackley, K., Adamcewicz, C., *et al.*, : GW231123: A Binary Black Hole Merger with Total Mass 190-265 M_{\odot} . *The Astrophysical Journal* **993**, 25 (2025) <https://doi.org/10.3847/2041-8213/ae0c9c>
- [97] Tagawa, H., Kocsis, B., Haiman, Z., Bartos, I., Omukai, K., *et al.*: Mass-gap Mergers in Active Galactic Nuclei. *The Astrophysical Journal* **908**, 194 (2021) <https://doi.org/10.3847/1538-4357/abd555>
- [98] Ford, K.E.S., McKernan, B.: Binary black hole merger rates in AGN discs versus nuclear star clusters: Loud beats quiet. *Monthly Notices of the Royal Astronomical Society* **517**, 5827–5834 (2022) <https://doi.org/10.1093/mnras/stac2861>
- [99] Graham, M.J., Ford, K.E.S., McKernan, B., Ross, N.P., Stern, D., *et al.*,

- : Candidate Electromagnetic Counterpart to the Binary Black Hole Merger Gravitational-Wave Event S190521g*. *Physical Review Letters* **124**, 251102 (2020) <https://doi.org/10.1103/PhysRevLett.124.251102>
- [100] Li, Y.-J., Tang, S.-P., Xue, L.-Q., Fan, Y.-Z.: GW231123: Likely a Product of Successive Mergers from ~ 10 Stellar-mass Black Holes. *The Astrophysical Journal* **999**, 127 (2026) <https://doi.org/10.3847/1538-4357/ae4102>
- [101] Delfavero, V., Ray, S., Cook, H.E., Nathaniel, K., McKernan, B., *et al.*, : Prospects for the Formation of GW231123 from the AGN Channel. *arXiv* (2025). <https://doi.org/10.48550/arXiv.2508.13412>
- [102] Kimball, C., Talbot, C., Berry, C.P.L., Carney, M., Zevin, M., *et al.*, : Black Hole Genealogy: Identifying Hierarchical Mergers with Gravitational Waves. *The Astrophysical Journal* **900**, 177 (2020) <https://doi.org/10.3847/1538-4357/aba518>
- [103] Stegmann, J., Olejak, A., de Mink, S.E.: Resolving Black Hole Family Issues among the Massive Ancestors of Very High-spin Gravitational-wave Events like GW231123. *The Astrophysical Journal* **992**, 26 (2025) <https://doi.org/10.3847/2041-8213/ae0e5f>
- [104] Abac, A.G., Abouelfettouh, I., Acernese, F., Ackley, K., Adamcewicz, C., *et al.*, : GW241011 and GW241110: Exploring Binary Formation and Fundamental Physics with Asymmetric, High-spin Black Hole Coalescences. *The Astrophysical Journal* **993**, 21 (2025) <https://doi.org/10.3847/2041-8213/ae0d54>
- [105] LIGO Scientific Collaboration, Virgo Collaboration, KAGRA Collaboration: GW241011 and GW241110: Exploring Binary Formation and Fundamental Physics with Asymmetric, High-spin Black Hole Coalescences. *Zenodo* (2025). <https://doi.org/10.5281/zenodo.17343574>
- [106] Pretorius, F.: Evolution of Binary Black-Hole Spacetimes. *Physical Review Letters* **95**, 121101 (2005) <https://doi.org/10.1103/PhysRevLett.95.121101>
- [107] Buonanno, A., Kidder, L.E., Lehner, L.: Estimating the final spin of a binary black hole coalescence. *Physical Review D* **77**, 026004 (2008) <https://doi.org/10.1103/PhysRevD.77.026004>
- [108] Guo, W.-H., Li, Y.-J., Wang, Y.-Z., Shao, Y., Wu, S.-C., *et al.*, : The Heavier the Faster: A Subpopulation of Heavy, Rapidly Spinning and Quickly Evolving Binary Black Holes. *The Astrophysical Journal* **975**, 54 (2024) <https://doi.org/10.3847/1538-4357/ad758a>
- [109] Farah, A.M., Vijaykumar, A., Fishbach, M.: The Steep Redshift Evolution of the Hierarchical Binary Black Hole Merger Rate May Cause the z - χ_{eff} Correlation. *The Astrophysical Journal* **1001**, 40 (2026) <https://doi.org/10.3847/2041-8213/>

- [110] Turbang, K., Lalleman, M., Callister, T.A., van Remortel, N.: The Metallicity Dependence and Evolutionary Times of Merging Binary Black Holes: Combined Constraints from Individual Gravitational-wave Detections and the Stochastic Background. *The Astrophysical Journal* **967**, 142 (2024) <https://doi.org/10.3847/1538-4357/ad3d5c>
- [111] Madau, P., Dickinson, M.: Cosmic Star-Formation History. *Annual Review of Astronomy and Astrophysics* **52**, 415–486 (2014) <https://doi.org/10.1146/annurev-astro-081811-125615>
- [112] Langer, N., Norman, C.A.: On the Collapsar Model of Long Gamma-Ray Bursts: Constraints from Cosmic Metallicity Evolution. *The Astrophysical Journal* **638**, 63–66 (2006) <https://doi.org/10.1086/500363>
- [113] Biscoveanu, S., Callister, T.A., Haster, C.-J., Ng, K.K.Y., Vitale, S., *et al.*: The Binary Black Hole Spin Distribution Likely Broadens with Redshift. *The Astrophysical Journal* **932**, 19 (2022) <https://doi.org/10.3847/2041-8213/ac71a8>
- [114] Adamcewicz, C., Thrane, E.: Do unequal-mass binary black hole systems have larger χ_{eff} ? Probing correlations with copulas in gravitational-wave astronomy. *Monthly Notices of the Royal Astronomical Society* **517**, 3928–3937 (2022) <https://doi.org/10.1093/mnras/stac2961>
- [115] Adamcewicz, C., Lasky, P.D., Thrane, E.: Evidence for a Correlation between Binary Black Hole Mass Ratio and Black Hole Spins. *The Astrophysical Journal* **958**, 13 (2023) <https://doi.org/10.3847/1538-4357/acf763>
- [116] Vijaykumar, A., Farah, A.M., Fishbach, M.: The Maximum Mass Ratio of Hierarchical Binary Black Hole Mergers May Cause the q - χ_{eff} Correlation. *The Astrophysical Journal* **999**, 30 (2026) <https://doi.org/10.3847/2041-8213/ae4878>
- [117] Abbott, B.P., Abbott, R., Abbott, T.D., Abernathy, M.R., Acernese, F., *et al.*, : Prospects for observing and localizing gravitational-wave transients with Advanced LIGO, Advanced Virgo and KAGRA. *Living Reviews in Relativity* **21**, 3 (2018) <https://doi.org/10.1007/s41114-018-0012-9>
- [118] Mandel, I., Farr, W.M., Gair, J.R.: Extracting distribution parameters from multiple uncertain observations with selection biases. *Monthly Notices of the Royal Astronomical Society* **486**, 1086–1093 (2019) <https://doi.org/10.1093/mnras/stz896>
- [119] Vitale, S., Gerosa, D., Farr, W.M., Taylor, S.R.: Inferring the Properties of

- a Population of Compact Binaries in Presence of Selection Effects. In: Handbook of Gravitational Wave Astronomy, p. 45 (2022). https://doi.org/10.1007/978-981-15-4702-7_45-1
- [120] Thrane, E., Talbot, C.: An introduction to Bayesian inference in gravitational-wave astronomy: Parameter estimation, model selection, and hierarchical models—Corrigendum. *Publications of the Astronomical Society of Australia* **37**, 036 (2020) <https://doi.org/10.1017/pasa.2020.23>
- [121] Essick, R.: Constructing Mixture Models for Sensitivity Estimates from Subsets of Separate Injections. *Research Notes of the American Astronomical Society* **5**, 220 (2021) <https://doi.org/10.3847/2515-5172/ac2ba7>
- [122] Tiwari, V.: Estimation of the sensitive volume for gravitational-wave source populations using weighted Monte Carlo integration. *Classical and Quantum Gravity* **35**, 145009 (2018) <https://doi.org/10.1088/1361-6382/aac89d>
- [123] Essick, R., Coughlin, M.W., Zevin, M., Chatterjee, D., Clarke, T.A., *et al.*, : Compact binary coalescence sensitivity estimates with injection campaigns during the LIGO-Virgo-KAGRA Collaborations’ fourth observing run. *Physical Review D* **112**, 102001 (2025) <https://doi.org/10.1103/44x3-hv3y>
- [124] Essick, R., Farr, W.: Precision Requirements for Monte Carlo Sums within Hierarchical Bayesian Inference. *arXiv* (2022). <https://doi.org/10.48550/arXiv.2204.00461>
- [125] Talbot, C., Golomb, J.: Growing pains: Understanding the impact of likelihood uncertainty on hierarchical Bayesian inference for gravitational-wave astronomy. *Monthly Notices of the Royal Astronomical Society* **526**, 3495–3503 (2023) <https://doi.org/10.1093/mnras/stad2968>
- [126] Heinzl, J., Vitale, S.: When (Not) to Trust Monte Carlo Approximations for Hierarchical Bayesian Inference. *arXiv* (2025). <https://doi.org/10.48550/arXiv.2509.07221>
- [127] Jones, M.C., Faddy, M.J.: A Skew Extension of the T-Distribution, with Applications. *Journal of the Royal Statistical Society Series B: Statistical Methodology* **65**(1), 159–174 (2003) <https://doi.org/10.1111/1467-9868.00378>
- [128] McKernan, B., Ford, K.E.S., O’Shaughnessy, R.: Black hole, neutron star, and white dwarf merger rates in AGN discs. *Monthly Notices of the Royal Astronomical Society* **498**, 4088–4094 (2020) <https://doi.org/10.1093/mnras/staa2681>
- [129] Gerosa, D., Berti, E.: Are merging black holes born from stellar collapse or previous mergers? *Physical Review D* **95**, 124046 (2017) <https://doi.org/10.1103/PhysRevD.95.124046>

- [130] Gerosa, D., De Renzi, V., Tettoni, F., Mould, M., Vecchio, A., *et al.*: Which Is Which? Identification of the Two Compact Objects in Gravitational-Wave Binaries. *Physical Review Letters* **134**, 121402 (2025) <https://doi.org/10.1103/PhysRevLett.134.121402>
- [131] Biscoveanu, S., Isi, M., Vitale, S., Varma, V.: New Spin on LIGO-Virgo Binary Black Holes. *Physical Review Letters* **126**, 171103 (2021) <https://doi.org/10.1103/PhysRevLett.126.171103>
- [132] Broekgaarden, F.S., Stevenson, S., Thrane, E.: Signatures of Mass Ratio Reversal in Gravitational Waves from Merging Binary Black Holes. *The Astrophysical Journal* **938**, 45 (2022) <https://doi.org/10.3847/1538-4357/ac8879>
- [133] Mould, M., Gerosa, D., Broekgaarden, F.S., Steinle, N.: Which black hole formed first? Mass-ratio reversal in massive binary stars from gravitational-wave data. *Monthly Notices of the Royal Astronomical Society* **517**, 2738–2745 (2022) <https://doi.org/10.1093/mnras/stac2859>
- [134] Fishbach, M., Holz, D.E.: Picky Partners: The Pairing of Component Masses in Binary Black Hole Mergers. *The Astrophysical Journal* **891**, 27 (2020) <https://doi.org/10.3847/2041-8213/ab7247>
- [135] Farah, A.M., Fishbach, M., Holz, D.E.: Two of a Kind: Comparing Big and Small Black Holes in Binaries with Gravitational Waves. *The Astrophysical Journal* **962**, 69 (2024) <https://doi.org/10.3847/1538-4357/ad0558>
- [136] Littenberg, T.B., Cornish, N.J., Lackeos, K., Robson, T.: Global analysis of the gravitational wave signal from Galactic binaries. *Physical Review D* **101**, 123021 (2020) <https://doi.org/10.1103/PhysRevD.101.123021>
- [137] The LIGO Scientific Collaboration, the Virgo Collaboration, the KAGRA Collaboration, Abac, A.G., Abouelfettouh, I., *et al.*, : GWTC-4.0: Updating the Gravitational-Wave Transient Catalog with Observations from the First Part of the Fourth LIGO-Virgo-KAGRA Observing Run. *arXiv* (2025). <https://doi.org/10.48550/arXiv.2508.18082>
- [138] LIGO Scientific Collaboration, Virgo Collaboration, KAGRA: GWTC-3: Compact Binary Coalescences Observed by LIGO and Virgo During the Second Part of the Third Observing Run — Parameter Estimation Data Release. *Zenodo* (2023). <https://doi.org/10.5281/zenodo.8177023>
- [139] Karnesis, N., Katz, M.L., Korsakova, N., Gair, J.R., Stergioulas, N.: Eryn: A multipurpose sampler for Bayesian inference. *Monthly Notices of the Royal Astronomical Society* **526**, 4814–4830 (2023) <https://doi.org/10.1093/mnras/stad2939>

- [140] Galaudage, S., Talbot, C., Thrane, E.: Gravitational-wave inference in the catalog era: Evolving priors and marginal events. *Physical Review D* **102**, 083026 (2020) <https://doi.org/10.1103/PhysRevD.102.083026>
- [141] Pedregosa, F., Varoquaux, G., Gramfort, A., Michel, V., Thirion, B., *et al.*, : Scikit-learn: Machine learning in Python. *Journal of Machine Learning Research* **12**, 2825–2830 (2011)
- [142] Cheng, A.Q.: RJpop Inference Results. Zenodo (2026). <https://doi.org/10.5281/zenodo.20273040>

	Parameter	Description	Prior
All	m_{\min}	Global minimum BH mass	$\mathcal{U}[3, 7]$
	\mathcal{R}_0	Local merger rate of each subpopulation	$\mathcal{U}[0.05, 100]$
	μ_χ	Mean of truncated Gaussian $p(\chi_{\text{eff}})$	$\mathcal{U}[-1, 1]$
	σ_χ	Width of truncated Gaussian $p(\chi_{\text{eff}})$	$\mathcal{U}[0.03, 1]$
skewt	μ_m	Peak location of $p_{\mathcal{S}}(m_1)$	$\mathcal{U}[6, 60]$
	σ_m	Scale parameter of $p_{\mathcal{S}}(m_1)$	$\mathcal{U}[1, 15]$
	$\log \alpha$	Tail weight parameter of $p_{\mathcal{S}}(m_1)$	$\mathcal{U}[-1, 2]$
	$\log \kappa$	Skewness parameter of $p_{\mathcal{S}}(m_1)$	$\mathcal{U}[-2, 2]$
NPLNP	α	Power-law index of $p_{\text{PL}}(m_1)$	$\mathcal{U}[1.1, 12]$
	p	Low-mass smoothing parameter of $p_{\text{PL}}(m_1)$	$\mathcal{U}[0.5, 5]$
	m_{\min}^{PL}	$p_{\text{PL}}(m_1)$ minimum	$\mathcal{U}[3, 50]$
	m_{\max}^{PL}	$p_{\text{PL}}(m_1)$ maximum	$\mathcal{U}[50, 300]$
	μ_m	Mean of Gaussian $p_{\mathcal{G}}(m_1)$	$\mathcal{U}[-1, 1]$
	σ_m	Width of Gaussian $p_{\mathcal{G}}(m_1)$	$\mathcal{U}[1, 10]$
All except skewt_ID	μ_q	Mean of truncated Gaussian $p(q)$	$\mathcal{U}[0.1, 1]$
	σ_q	Width of truncated Gaussian $p(q)$	$\mathcal{U}[0.1, 1]$
skewt_ID	ρ	$m_1 - m_2$ Gaussian copula correlation	$\mathcal{U}[-1, 1]$
skewt_m2max	$m_{2,\max}$	Global secondary mass maximum	$\mathcal{U}[40, 200]$
All except skewt_z	γ	Global redshift power law index	$\mathcal{U}[-6, 6]$
skewt_z	γ	Subpopulation redshift power law index	$\mathcal{U}[-6, 10]$

Table 1: Population parameters of all of our population models, as well as their prior ranges in the inference. \mathcal{U} denotes a uniform distribution; masses are quoted in M_\odot and rates in $\text{Gpc}^{-3} \text{yr}^{-1}$.

7 Extended Data Figures

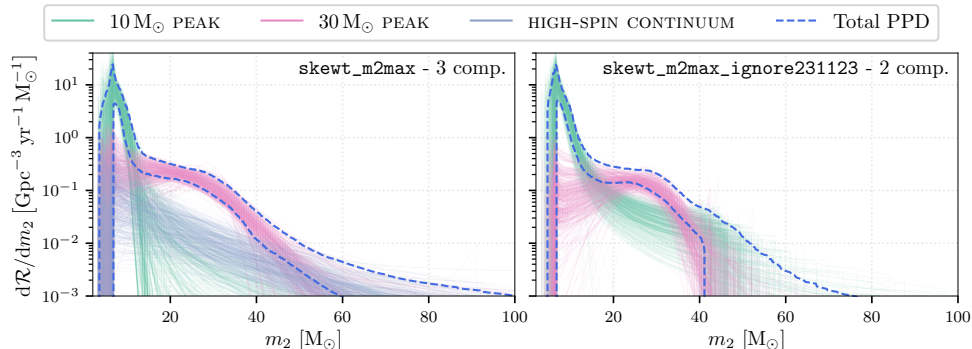
This section presents supplementary figures referenced throughout the main text.

In Extended Data Fig. 1, we show the differential merger rate in m_2 inferred from the `skewt_m2max` population model allowing for a secondary mass maximum, including (left) and excluding (right) GW231123. As seen in the right panel, we do indeed find evidence for a steep drop-off around $50 M_\odot$ in the secondary-mass distribution when GW231123 is excluded, consistent with the PISN gap. Nonetheless, the non-existence of a gap or maximum is not completely ruled out, with $m_{2,\max} = 48_{-7}^{+14} M_\odot$. Because GW231123 almost certainly belongs to the high-spin continuum subpopulation, excluding it from the inference is sufficient for the data to mildly prefer the simpler 2-component model over a 3-component model ($\mathcal{B} = 2.7$, compared to $\mathcal{B} = 0.6$ when GW231123 is included). This shows that individual events can significantly impact smaller subpopulations, such as the high-spin continuum, which constitutes only $\approx 2\%$ of the underlying population.

[‡]Without GW231123.

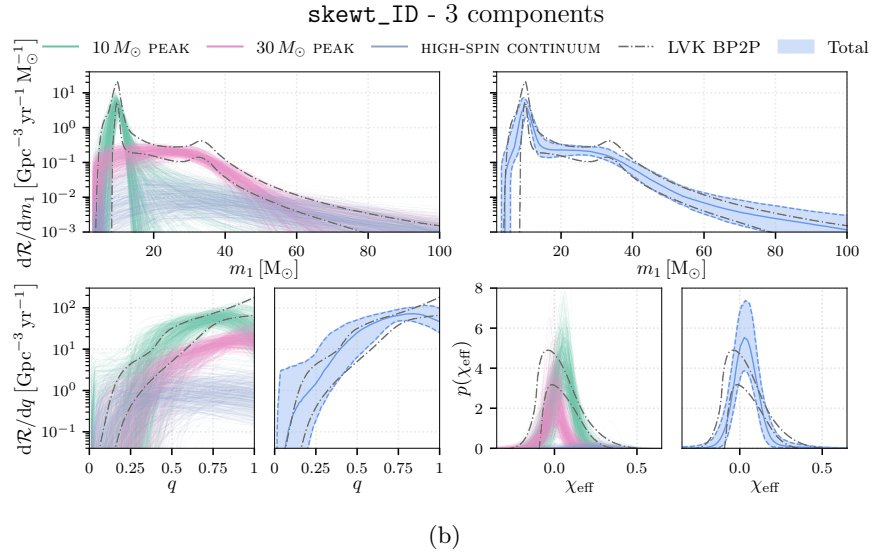
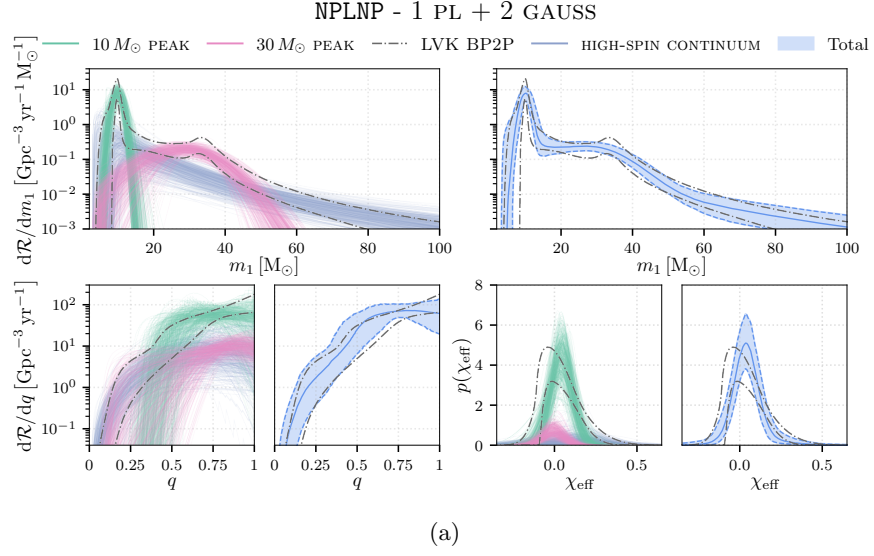
Model	skewt	skewt_ID	skewt_z	skewt_m2max	skewt_m2max [‡]	Model	NPLNP
$n = 2$	0.77	0.37	1.6	0.62	1.4	1 PL, 1 gauss	0.08
$n = 3$	1	1	1	1	1	1 PL, 2 gauss	1
	-	-	-	-	-	2 PL, 1 gauss	0.62
$n = 4$	0.01	0.01	0.02	0.01	0.01	2 PL, 2 gauss	0.02

Table 2: Bayes factors between models of varying complexity within each of our population models, relative to the 1 PL + 2 Gaussian model of NPLNP (right two columns) and the 3-component model of all other population models.

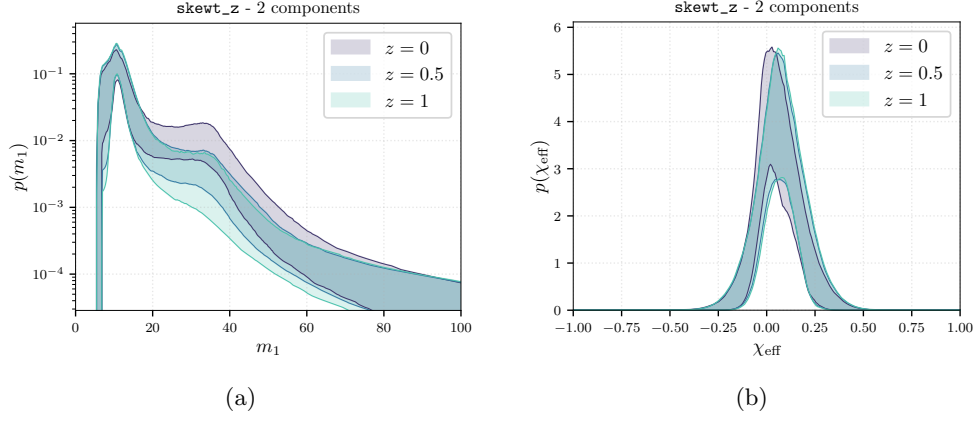


Extended Data Fig. 1 Posterior draws from the marginal differential merger rate as a function of m_2 at $z = 0.2$ for each subpopulation, inferred with (left) and without (right) GW231123. The 90% credibility interval of the total rate is overplotted with the dashed blue lines.

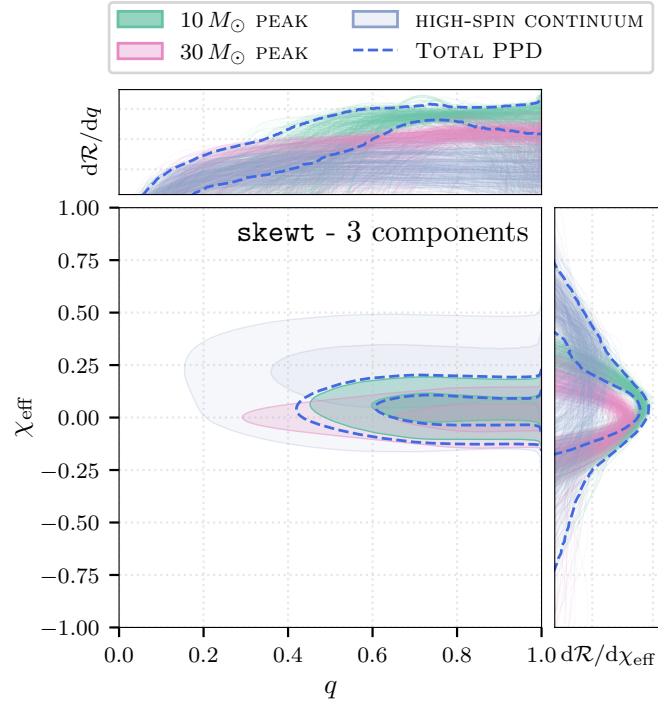
Next, Extended Data Fig. 2 shows the posterior marginals of m_1 , q , and χ_{eff} for the NPLNP and `skewt_ID` population models. Together with Fig. 1, these results demonstrate the robustness of our three identified subpopulations across the different population models. Extended Data Fig. 3 shows the inferred primary mass and χ_{eff} distributions at $z = 0, 0.5, \text{ and } 1$ under the `skewt_z` model. Because the $10 M_{\odot}$ peak and continuum evolves faster than the $30 M_{\odot}$ peak, the latter becomes subdominant to the former at higher redshifts. Furthermore, we find no evidence for the broadening of the χ_{eff} distribution with redshift, as we discussed in Section 4. Finally, Extended Data Fig. 4 shows joint q - χ_{eff} contours of each subpopulation in the `skewt` population model, where we also find no significant q - χ_{eff} correlation.



Extended Data Fig. 2 The same as Fig. 1 but for the NPLNP (a) and skewt_ID (b) population models.



Extended Data Fig. 3 90% credibility intervals on the marginal distributions of (a) m_1 and (b) χ_{eff} at $z = 0$, $z = 0.5$, and $z = 1$.



Extended Data Fig. 4 50% and 90% contours of the median posterior $d\mathcal{R}^k/dq d\chi_{\text{eff}}$ for each subpopulation k , evaluated at $z = 0.2$ in the **skewt** model; opacity of the shading corresponds to the relative rates of the subpopulations. Corresponding posterior sample draws of the marginalized 1D distributions (in log-scale) are shown in the side panels.